



Available online at www.sciencedirect.com

ScienceDirect

Comput. Methods Appl. Mech. Engrg. 396 (2022) 115018

Computer methods in applied mechanics and engineering

www.elsevier.com/locate/cma

State-space Bloch mode synthesis for fast band-structure calculations of non-classically damped phononic materials

Abdulaziz Aladwani^{a,*}, Mostafa Nouh^b, Mahmoud I. Hussein^{c,d,**}

^a Department of Manufacturing Engineering Technology, College of Technological Studies, Shuwaikh 70654, Kuwait
 ^b Department of Mechanical and Aerospace Engineering, University at Buffalo (SUNY), Buffalo, NY 14260, United States of America
 ^c Ann and HJ Smead Department of Aerospace Engineering Sciences, University of Colorado Boulder, Boulder, CO 80303,
 United States of America

d Department of Physics, University of Colorado Boulder, Boulder, CO 80303, United States of America

Received 19 December 2021; received in revised form 19 March 2022; accepted 13 April 2022 Available online 24 May 2022

Abstract

Bloch mode synthesis (BMS) techniques enable efficient band-structure calculations of periodic media by forming reduced-order models of the unit cell. Rooted in the framework of the Craig-Bampton component mode synthesis methodology, these techniques decompose the unit cell into interior and boundary degrees-of-freedom that are nominally described, respectively, by sets of normal modes and constraint modes. In this paper, we generalize the BMS approach by state-space transformation to extend its applicability to generally damped periodic materials that violate the Caughey-O'Kelly condition for classical damping. In non-classically damped periodic models, the fixed-interface eigenvalue problem may, in general, produce a mixture of underdamped and overdamped modes. We examine two mode-selection schemes for the reduced-order model and demonstrate the underlying accuracy-efficiency trade-offs when qualitatively distinct mixtures of underdamped and overdamped modes are incorporated. The proposed approach provides a highly effective computational tool for analysis of large models of phononic crystals and acoustic/elastic metamaterials with complex damping properties.

© 2022 Elsevier B.V. All rights reserved.

Keywords: Phononic crystals; Metamaterials; Non-classical damping; Reduced-order modeling; Bloch mode synthesis; State-space formulation

1. Introduction

The development of artificial materials with periodically arranged properties and/or geometric features has opened up a wide range of opportunities in acoustics and elastodynamics over the past few decades [1,2]. The fundamental wave propagation characteristics in these materials are described by the band structure (dispersion curves)—a frequency versus wave vector relation obtained by application of Bloch's theorem [3] and usually computed using a numerical technique such as the finite-element method [4–6]. For waveguides with material/geometric complexities

E-mail addresses: ae.aladwani@paaet.edu.kw (A. Aladwani), mih@colorado.edu (M.I. Hussein).

^{*} Correspondence to: Department of Manufacturing Engineering Technology, College of Technological Studies, Shuwaikh 70654, Kuwait.

^{**} Corresponding author at: Ann and HJ Smead Department of Aerospace Engineering Sciences, University of Colorado Boulder, Boulder, CO 80303, United States of America.

(including periodicity) across the cross section but a uniform configuration along the direction of wave propagation, the Wave Finite-Element (WFE) method [7,8] is commonly used for dispersion curves computation.

The compelling spatial wave attenuation behavior offered by periodic materials is a conservative phenomenon, i.e., it is attained without the aid of dissipative elements. However, the incorporation of damping in models of periodic materials not only provides a more realistic description, but also enables the realization of unique wave attenuation properties in both time [9-16] and space [12,17,18]. For damping models that satisfy the Caughey-O'Kelly condition [19], such as Rayleigh (proportional) damping [20], classical modal analysis is executed straightforwardly for the Bloch problem [6]. Non-classical damping models, on the other hand, require more in-depth treatment. In the structural dynamics literature, several studies provided generalized modal decomposition schemes for diagonalization of the damping matrix in the emerging models, commonly using state-space transformation which reduces the order of the problem while doubling its size [21-23]. Analogously, the state-space framework has been utilized for band-structure calculations of periodic materials with general, non-classical damping models [10,15]. Alternatively, a model is set up as a quadratic eigenvalue problem geared to solving for the wave vectors as a function of prescribed real values of frequency (i.e., the $\kappa(\omega)$ problem), thus readily incorporating damping models with arbitrary complexities [17,18]. Another approach that avoids state-space representation is the Bloch-Rayleigh perturbation method where the complex eigensolution is approximated by Bloch wave basis functions of a corresponding undamped unit cell [24]. In one dimension, the transfer-matrix method may be readily adapted to treat models with complex damping and provide dispersion band structures based on frequencies and wave numbers that are simultaneously complex [25].

Often the unit-cell model is large in terms of its number of degrees-of-freedom (DOFs) representation, which causes significant computational costs for band-structure calculations, especially when the evaluation is required across numerous points in the Brillouin zone (BZ), as in, for example, topological phononics [26–30], or when the calculations are repeated numerous times as in unit-cell topology optimization [4,31–33]. Band-sorting algorithms also consume large computational effort [34].

In other fields that involve band-structure analysis, such as electrodynamics, techniques evolved for speeding-up the band-structure calculations. Using a Bloch modal reduction framework for electronic structure calculations, Shirley created a reduced modal matrix assembled by solving the full eigenproblem at certain wave vector points (κ -points) of interest in the BZ and used it to efficiently diagonalize the problem at other κ -points [35]. Hussein extended this methodology to phononic and photonic band structures and introduced a Bloch mode selection scheme where the reduced basis is formed from eigenvectors corresponding to high-symmetry points for the crystal structure. This technique is called Reduced Bloch Mode Expansion (RBME) [6]. Bloch mode selection at high-symmetry points was done in an earlier study involving a multiscale assumed-strain projection method [36]. Bloch mode selection in frequency space was also proposed [37].

An alternative track for modal reduction of the Bloch problem is based on the component mode synthesis (CMS) methodology [38,39]. In this methodology, which is well-established in the structural dynamics field, a finite structural model is divided into components where each is reduced separately by fixed-interface modal analysis, and complemented by constraint modes to account for the interfaces between the components. A reduced-order model for the complete structure is then reassembled. This approach has been utilized for the infinite-structure band-structure calculation problem by dissecting the unit cell into interior and boundary DOFs for which sets of normal modes and constraint modes are calculated [40]. The approach was later adopted by Krattiger and Hussein and analyzed for its trade-off between accuracy and efficiency for phononic materials and also extended to incorporate boundary modes reduction [41]. Termed Bloch Mode Synthesis (BMS), the methodology has since experienced various developments. Zhou et al. implemented it on two-dimensional (2D) periodic structures showing slowness surfaces and energy flow vector fields [42]. Palermo and Marzani extended the methodology to the $\kappa(\omega)$ problem, referred to as Extended BMS (EBMS) [43] and Krattiger and Hussein enriched it with residual modes and local boundary reduction that is independent of κ , giving rise to the Generalized BMS (GBMS) method [44]. Xi and Zheng augmented GBMS with algebraic condensation (AC), yielding the GBMS-AC version of the method [45]. Hajarolasvadi and Elbanna applied BMS to study waveguides connected in parallel [46]. Recently, Cool et al. investigated the effect of unit-cell choice on BMS and GBMS performance [47]. Utilization of CMS analysis for dispersion curves calculations was also applied to the WFE method for 1D waveguides [48,49] and 2D waveguides [50]. The technique by Fan et al. involved various free-interface CMS approaches [49].

Originally developed to deal with undamped models of finite structures, the CMS framework has also been extended to the analysis of damped finite structures, including non-classically damped models where state-space

transformation has been utilized in conjunction with fixed-interface methods [51–53] or free-interface methods [54–56]. The reader is referred to Gruber and Rixen [57] and Gruber et al. [58] for overviews of various CMS strategies for models with arbitrary damping, and to Domenico and Ricciardi for an analysis of two measures for quantifying the modal participation and mode selection considering non-classically damped models that encompass mixed damping, i.e., underdamped and overdamped modes [59]. Also of interest is a recent investigation of a version of the Hasselman and Kaplan approach using free-interface CMS [60]. While the aforementioned state-space CMS methods have been widely used to analyze finite structures from a structural vibrations perspective, these methods are yet to be investigated in the context of wave propagation and Bloch analysis pertaining to periodic materials.

In this paper, we present a state-space generalization of the BMS method to incorporate general non-classical damping. Furthermore, given the nontrivial modal participation of complex damped modes, we device two distinct schemes of damped mode selection for the reduced-order model. We evaluate the accuracy and computational savings of the new approach, based on each scheme, on an example of a phononic crystal [61,62] and an example of a locally resonant elastic metamaterial [63]. Finally, we conclude with a "big picture" characterization of performance by showing accuracy–efficiency maps pertaining to each damped mode-selection scheme.

2. Band-structure computation

In this section, we briefly review the mathematical foundation for computing the band structures of damped infinite periodic models in their complete (unreduced) form. Consider a free unit cell of a periodic medium for which the finite-element equations of motion are written as

$$\mathbf{M}\ddot{\mathbf{u}}(t) + \mathbf{D}\dot{\mathbf{u}}(t) + \mathbf{K}\mathbf{u}(t) = \mathbf{0} \tag{1}$$

where \mathbf{u} is a *N*-dimensional vector collecting the *N* free displacements of the unit cell, \mathbf{M} , \mathbf{D} , and \mathbf{K} are the $N \times N$ mass, damping, and stiffness matrices, respectively. For plane time harmonic waves of the form $\mathbf{u}(t) = \overline{\mathbf{u}} \exp{(\lambda t)}$, Eq. (1) can be rewritten as $(\mathbf{K} + \lambda \mathbf{D} + \lambda^2 \mathbf{M}) \overline{\mathbf{u}} = \mathbf{0}$, where λ is a complex-valued function that permits temporal wave attenuation. The vector $\overline{\mathbf{u}}$ can be divided into interior $\overline{\mathbf{u}}_I$ and interface $\overline{\mathbf{u}}_A$ DOFs (see Fig. 1), i.e., $\overline{\mathbf{u}} = \{\overline{\mathbf{u}}_I^T \ \overline{\mathbf{u}}_A^T\}^T$ and the interface DOFs can be partitioned such that

$$\overline{\mathbf{u}}_{A} = \left\{ \overline{\mathbf{u}}_{L}^{T} \quad \overline{\mathbf{u}}_{R}^{T} \quad \overline{\mathbf{u}}_{R}^{T} \quad \overline{\mathbf{u}}_{LB}^{T} \quad \overline{\mathbf{u}}_{RB}^{T} \quad \overline{\mathbf{u}}_{LT}^{T} \quad \overline{\mathbf{u}}_{RT}^{T} \right\}^{T}$$

$$(2)$$

where the notation $(\cdot)^T$ denotes the transpose quantity of (\cdot) . For plane waves in a periodic material, Bloch's theorem [3] provides the following relationships

$$\overline{\mathbf{u}}_{R} = \overline{\mathbf{u}}_{L}\alpha_{1}, \quad \overline{\mathbf{u}}_{T} = \overline{\mathbf{u}}_{B}\alpha_{2}, \quad \overline{\mathbf{u}}_{RB} = \overline{\mathbf{u}}_{LB}\alpha_{1}, \quad \overline{\mathbf{u}}_{LT} = \overline{\mathbf{u}}_{LB}\alpha_{2}, \quad \overline{\mathbf{u}}_{RT} = \overline{\mathbf{u}}_{LB}\alpha_{1}\alpha_{2} \tag{3}$$

between the unit-cell boundaries, where $\alpha_1 = e^{j \kappa^T \mathbf{r}_1}$ and $\alpha_2 = e^{j \kappa^T \mathbf{r}_2}$, with $\kappa = \left\{ \kappa_x \quad \kappa_y \right\}^T$ being the wave vector, \mathbf{r}_1 and \mathbf{r}_2 are primitive translational vectors of the unit cell, and $j = \sqrt{-1}$. Eq. (3) imposes a set of periodic boundary conditions that can be expressed as $\overline{\mathbf{u}} = \mathbf{P}\widetilde{\mathbf{u}}$, where $\widetilde{\mathbf{u}} = \left\{ \overline{\mathbf{u}}_I^T \quad \overline{\mathbf{u}}_L^T \quad \overline{\mathbf{u}}_B^T \quad \overline{\mathbf{u}}_{LB}^T \right\}^T$ is a N_P -dimensional vector with only periodic displacements and

$$\mathbf{P}(\mathbf{\kappa}) = \begin{bmatrix} \mathbf{I}_{\mathrm{I}} & \mathbf{0} & \mathbf{0} & \mathbf{0} \\ \mathbf{0} & \mathbf{I}_{\mathrm{L}} & \mathbf{0} & \mathbf{0} \\ \mathbf{0} & \alpha_{1} \mathbf{I}_{\mathrm{R}} & \mathbf{0} & \mathbf{0} \\ \mathbf{0} & \mathbf{0} & \mathbf{I}_{\mathrm{B}} & \mathbf{0} \\ \mathbf{0} & \mathbf{0} & \alpha_{2} \mathbf{I}_{\mathrm{T}} & \mathbf{0} \\ \mathbf{0} & \mathbf{0} & \mathbf{0} & \mathbf{I}_{\mathrm{LB}} \\ \mathbf{0} & \mathbf{0} & \mathbf{0} & \alpha_{1} \mathbf{I}_{\mathrm{RB}} \\ \mathbf{0} & \mathbf{0} & \mathbf{0} & \alpha_{2} \mathbf{I}_{\mathrm{LT}} \\ \mathbf{0} & \mathbf{0} & \mathbf{0} & \alpha_{1} \alpha_{2} \mathbf{I}_{\mathrm{RT}} \end{bmatrix}$$

$$(4)$$

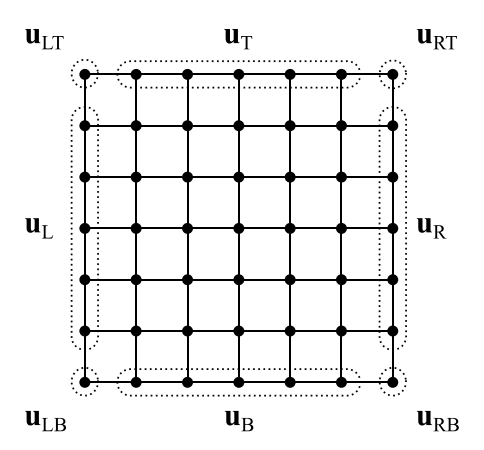


Fig. 1. A 2D unit cell with partitioned boundary sets.

is the Bloch periodicity matrix; **I** and **0** are identity and null matrices of proper sizes. Upon enforcing the Bloch periodicity boundary conditions, the following quadratic eigenvalue problem is obtained

$$\left[\widetilde{\mathbf{K}}(\mathbf{\kappa}) + \lambda(\mathbf{\kappa})\widetilde{\mathbf{D}}(\mathbf{\kappa}) + \lambda^{2}(\mathbf{\kappa})\widetilde{\mathbf{M}}(\mathbf{\kappa})\right]\widetilde{\mathbf{u}}(\mathbf{\kappa}) = \mathbf{0}$$
(5)

where $\widetilde{\mathbf{M}} = \mathbf{P}^H \mathbf{M} \mathbf{P}$, $\widetilde{\mathbf{D}} = \mathbf{P}^H \mathbf{D} \mathbf{P}$, and $\widetilde{\mathbf{K}} = \mathbf{P}^H \mathbf{K} \mathbf{P}$ are $N_P \times N_P$ wave vector-dependent matrices and \mathbf{P}^H is the Hermitian transpose of the Bloch periodicity matrix. By state-space transformation, the quadratic eigenvalue problem in Eq. (5) can be expressed as the following linear eigenvalue problem [10,15]:

$$\left[\lambda(\kappa)\widetilde{A}(\kappa) + \widetilde{B}(\kappa)\right]\widetilde{y}(\kappa) = 0 \tag{6}$$

where $\widetilde{\mathbf{y}} = [\widetilde{\mathbf{u}}^{\mathrm{T}} \quad \lambda \widetilde{\mathbf{u}}^{\mathrm{T}}]^{\mathrm{T}}$ is a $2N_{\mathrm{P}}$ -dimensional eigenvector and

$$\widetilde{A}(\kappa) = \begin{bmatrix} \widetilde{D}(\kappa) & \widetilde{M}(\kappa) \\ \widetilde{M}(\kappa) & 0 \end{bmatrix} \quad \text{and} \quad \widetilde{B}(\kappa) = \begin{bmatrix} \widetilde{K}(\kappa) & 0 \\ 0 & -\widetilde{M}(\kappa) \end{bmatrix}$$
 (7)

are the $2N_P \times 2N_P$ state-space matrices. In general, the solution of Eq. (6) yields a mixture of (1) $2N_U$ underdamped (oscillatory) modes with complex conjugate pairs of eigenvalues and eigenvectors and (2) $2N_O$ overdamped (non-oscillatory) modes that are associated with real-valued eigenvalues and eigenvectors, such that $2N_P = 2N_U + 2N_O$. The underdamped modes can be explicitly expressed as

$$\widetilde{\mathbf{y}}_{n}, \ \widetilde{\mathbf{y}}_{n}^{*} = \boldsymbol{\psi}_{n} \pm j\boldsymbol{\chi}_{n}, \quad \lambda_{n}, \ \lambda_{n}^{*} = -\zeta_{n}\omega_{r,n} \pm j\omega_{d,n}, \quad \text{with}$$

$$\omega_{r,n} = |\lambda_{n}| = \sqrt{(\mathbf{Re}(\lambda_{n}))^{2} + (\mathbf{Im}(\lambda_{n}))^{2}}, \quad \zeta_{n} = -\frac{\mathbf{Re}(\lambda_{n})}{|\lambda_{n}|}, \quad \omega_{d,n} = \mathbf{Im}(\lambda_{n}) = \omega_{r,n}\sqrt{1 - \zeta_{n}^{2}}$$
(8)

whereas the overdamped modes (if they exist) can be written as

$$\widetilde{\mathbf{y}}_{m}, \ \widetilde{\mathbf{y}}_{m+N_{\mathrm{O}}} = \boldsymbol{\psi}_{m}, \ \boldsymbol{\psi}_{m+N_{\mathrm{O}}}, \quad \boldsymbol{\chi}_{m}, \ \boldsymbol{\chi}_{m+N_{\mathrm{O}}} = \mathbf{0}, \quad \lambda_{m}, \lambda_{m+N_{\mathrm{O}}} = -\zeta_{m}\omega_{r,m} \pm \omega_{d,m} < 0, \quad \text{with}$$

$$\omega_{r,m} = \sqrt{\lambda_{m}\lambda_{m+N_{\mathrm{O}}}}, \quad \zeta_{m} = -(\lambda_{m} + \lambda_{m+N_{\mathrm{O}}})/2\sqrt{\lambda_{m}\lambda_{m+N_{\mathrm{O}}}}, \quad \omega_{d,m} = (\lambda_{m} - \lambda_{m+N_{\mathrm{O}}})/2 = \omega_{r,m}\sqrt{\zeta_{m}^{2} - 1}$$
(9)

where $n=1,2\ldots,N_{\rm U},\ m=1,2\ldots,N_{\rm O}$, and the notations ${\bf Re}\,(\cdot)$, ${\bf Im}\,(\cdot)$, and $(\cdot)^*$ denote the real, imaginary, and complex conjugate quantities of (\cdot) , respectively. For underdamped modes, ω_r , ω_d , and ζ are the resonant frequency, damped frequency, and damping ratio, respectively, while ψ_n and χ_n are couples of real-valued vectors. The eigenvalues are ordered such that $|\lambda_1|<|\lambda_2|<\cdots<|\lambda_{2N_{\rm P}}|$ and the corresponding eigenvectors follow the same order. It should be noted that all the parameters in Eqs. (8) and (9) are wave vector-dependent. However, this dependence is not shown in both equations to simplify the notation. Finally, it is worthy to mention that when computing the band structures of a given unit cell without model reduction (i.e., using full-order model), only the underdamped modes are usually computed (using Eq. (8)) because the primary goal is to investigate the structural behavior in the oscillatory frequency range (i.e., for $0 < \zeta_n < 1$). Consequently, Eq. (9) is typically ignored as part of the solution obtained from the eigenvalue problem in Eq. (6). Despite their minor importance in most practical

vibration problems, overdamped modes truncation effects on the accuracy of reduced-order models will be discussed later.

3. Classical Bloch mode synthesis versus state-space Bloch mode synthesis

Bloch mode synthesis methods are projection-based model order reduction strategies for periodic structures [40–45]. They are a natural extension of the CMS methods which have been widely used to simplify and speed-up the analysis of complicated finite element structural models. The original (classical) BMS framework was laid out based on the Craig–Bampton approach which simplifies the internal dynamics of a given unit cell using a set of real-valued fixed-interface modes.

3.1. Classical Bloch mode synthesis

In classical BMS, the damping matrix \mathbf{D} is neglected in the reduction process and the undamped equations of motion are partitioned as follows

$$\begin{bmatrix} \mathbf{M}_{\mathrm{II}} & \mathbf{M}_{\mathrm{IA}} \\ \mathbf{M}_{\mathrm{AI}} & \mathbf{M}_{\mathrm{AA}} \end{bmatrix} \begin{Bmatrix} \ddot{\mathbf{u}}_{\mathrm{I}}(t) \\ \ddot{\mathbf{u}}_{\mathrm{A}}(t) \end{Bmatrix} + \begin{bmatrix} \mathbf{K}_{\mathrm{II}} & \mathbf{K}_{\mathrm{IA}} \\ \mathbf{K}_{\mathrm{AI}} & \mathbf{K}_{\mathrm{AA}} \end{bmatrix} \begin{Bmatrix} \mathbf{u}_{\mathrm{I}}(t) \\ \mathbf{u}_{\mathrm{A}}(t) \end{Bmatrix} = \mathbf{0}$$
(10)

For a fixed-interface unit cell, Eq. (10) reduces to $\mathbf{M}_{\mathrm{II}}\ddot{\mathbf{u}}_{\mathrm{I}}(t) + \mathbf{K}_{\mathrm{II}}\mathbf{u}_{\mathrm{I}}(t) = \mathbf{0}$, which in combination with the solution $\mathbf{u}_{\mathrm{I}}(t) = \overline{\mathbf{u}}_{\mathrm{I}} \exp(j\omega t)$, can be used to set-up the eigenvalue problem

$$\mathbf{K}_{\mathrm{II}}\mathbf{\Phi}_{\mathrm{I}} = \mathbf{M}_{\mathrm{II}}\mathbf{\Phi}_{\mathrm{I}}\mathbf{\Omega}_{\mathrm{I}}, \quad \text{with} \quad \mathbf{\Phi}_{\mathrm{I}} = \begin{bmatrix} \overline{\mathbf{u}}_{\mathrm{I}}^{1} & \overline{\mathbf{u}}_{\mathrm{I}}^{2} & \cdots & \overline{\mathbf{u}}_{\mathrm{I}}^{N_{\mathrm{I}}} \end{bmatrix} \quad \text{and} \quad \mathbf{\Omega}_{\mathrm{I}} = \operatorname{diag}\left[\omega_{k}^{2}\right]$$
(11)

where $k=1,2,\ldots,N_{\rm I}$, ω_k^2 is the kth real-valued eigenvalue and $\overline{\bf u}_{\rm I}^k$ is the corresponding kth eigenvector. The matrix $\Phi_{\rm I}$ is the $N_{\rm II} \times N_{\rm I}$ fixed-interface modal matrix collecting the real-valued eigenvectors up to the $N_{\rm I}$ th mode ($N_{\rm I}$ is the number of modes retained in the reduced-order model which is much smaller than the original internal dimension $N_{\rm II}$). The matrix $\Omega_{\rm I}$ is the corresponding $N_{\rm I} \times N_{\rm I}$ reduced spectral matrix, which contains the squared natural frequencies on its diagonal. Next, a set of constraint modes of the form

$$\Psi = -\mathbf{K}_{\Pi}^{-1}\mathbf{K}_{\mathrm{IA}} \tag{12}$$

is used to describe the influence of the interface motion on the internal dynamics. From Eqs. (11) and (12), the free displacements vector can be approximated using the following transformation of coordinates

$$\mathbf{u}(t) = \begin{cases} \mathbf{u}_{\mathrm{I}}(t) \\ \mathbf{u}_{\mathrm{A}}(t) \end{cases} = \underbrace{\begin{bmatrix} \mathbf{\Phi}_{\mathrm{I}} & \mathbf{\Psi} \\ \mathbf{0} & \mathbf{I} \end{bmatrix}}_{\mathbf{T}_{\mathrm{CR}}} \underbrace{\begin{cases} \boldsymbol{\eta}_{\mathrm{I}}(t) \\ \mathbf{u}_{\mathrm{A}}(t) \end{cases}}_{\mathbf{u}_{\mathrm{r}}(t)}$$
(13)

where η_I contains the modal coordinates that describe the internal dynamics of the unit cell and T_{CB} is the Craig-Bampton transformation matrix. For reasons that will be clarified later, we explicitly expand the first row of Eq. (13) and its time derivative, i.e.,

Substituting Eq. (13) into Eq. (1) in its partitioned form and pre-multiplying Eq. (1) by \mathbf{T}_{CB}^T , the reduced-order model equations become $M\ddot{\mathbf{u}}_r(t) + D\dot{\mathbf{u}}_r(t) + K\mathbf{u}_r(t) = \mathbf{0}$, where $M = \mathbf{T}_{CB}^T \mathbf{M} \mathbf{T}_{CB}$, $D = \mathbf{T}_{CB}^T \mathbf{D} \mathbf{T}_{CB}$, and $K = \mathbf{T}_{CB}^T \mathbf{K} \mathbf{T}_{CB}$ are the reduced matrices and \mathbf{u}_r is the reduced free displacements vector. Finally, the steps outlined in Section 2 for (1) applying the Bloch periodicity boundary conditions and (2) computing the frequency and damping ratio band structures of full-order models can be straightforwardly extended to reduced-order models, provided that the system is classically damped [9]. This is however not the case if the system is non-classically damped, as will be shown later. The classical BMS method outlined in this section has been widely (and efficiently) used to compute the dispersion curves of undamped periodic systems. We note that the same method can also be used to deal with classically damped periodic systems. Classically damped systems are those systems where the damping matrix \mathbf{D} meets the following Caughey–O'Kelly condition

$$\mathbf{D}\mathbf{M}^{-1}\mathbf{K} = \mathbf{K}\mathbf{M}^{-1}\mathbf{D} \tag{15}$$

If Eq. (15) is satisfied, the eigensolutions of a given damped system directly correlate with the natural modes of the system in its undamped form. A proportionally damped system represents an example that satisfies Eq. (15). On the other hand, systems with arbitrary viscous damping violate Eq. (15). Consequently, the use of real-valued eigenvectors in such non-classically damped systems do not decouple the equations of motion when transformed into modal coordinates, i.e., leaving some non-zero off-diagonal terms in the transformed damping matrix. For non-classically damped systems, the equations of motion can be successfully decoupled using a complex-valued reduction basis that arises from solving an eigenvalue problem in the state-space as will be shown next.

3.2. State-space Bloch mode synthesis

If the system is non-classically damped, the classical model order reduction process outlined in the preceding section is not applicable. Therefore, a complex-valued reduction basis should be derived in the augmented state variable space, i.e., $A\dot{y}(t) + By(t) = 0$. First, the previous equation is partitioned as follows

$$\begin{bmatrix} \mathbf{A}_{\mathrm{II}} & \mathbf{A}_{\mathrm{IA}} \\ \mathbf{A}_{\mathrm{AI}} & \mathbf{A}_{\mathrm{AA}} \end{bmatrix} \begin{pmatrix} \dot{\mathbf{y}}_{\mathrm{I}}(t) \\ \dot{\mathbf{y}}_{\mathrm{A}}(t) \end{pmatrix} + \begin{bmatrix} \mathbf{B}_{\mathrm{II}} & \mathbf{B}_{\mathrm{IA}} \\ \mathbf{B}_{\mathrm{AI}} & \mathbf{B}_{\mathrm{AA}} \end{bmatrix} \begin{pmatrix} \mathbf{y}_{\mathrm{I}}(t) \\ \mathbf{y}_{\mathrm{A}}(t) \end{pmatrix} = \mathbf{0}$$
(16)

which yields fixed-interface equations of the form

$$\mathbf{A}_{\Pi}\dot{\mathbf{y}}_{\Pi}(t) + \mathbf{B}_{\Pi}\mathbf{y}_{\Pi}(t) = \mathbf{0} \tag{17}$$

where \mathbf{y}_{I} denotes the $2N_{\mathrm{II}}$ -dimensional fixed-interface state vector, and \mathbf{A}_{II} and \mathbf{B}_{II} are the corresponding $2N_{\mathrm{II}} \times 2N_{\mathrm{II}}$ state-space matrices, expressed as

$$\mathbf{y}_{\mathrm{I}}(t) = \begin{cases} \mathbf{u}_{\mathrm{I}}(t) \\ \dot{\mathbf{u}}_{\mathrm{I}}(t) \end{cases}, \quad \mathbf{A}_{\mathrm{II}} = \begin{bmatrix} \mathbf{D}_{\mathrm{II}} & \mathbf{M}_{\mathrm{II}} \\ \mathbf{M}_{\mathrm{II}} & \mathbf{0} \end{bmatrix}, \quad \mathbf{B}_{\mathrm{II}} = \begin{bmatrix} \mathbf{K}_{\mathrm{II}} & \mathbf{0} \\ \mathbf{0} & -\mathbf{M}_{\mathrm{II}} \end{bmatrix}$$
(18)

By substituting the solution $\mathbf{y}_{\rm I}(t) = \overline{\mathbf{y}}_{\rm I} \exp{(\lambda t)}$ into Eq. (17), the state-space eigenvalue problem

$$\mathbf{B}_{\mathrm{II}}\overline{\Phi}_{\mathrm{I}} = \mathbf{A}_{\mathrm{II}}\overline{\Phi}_{\mathrm{I}}\Lambda_{\mathrm{I}} \tag{19}$$

is obtained, where $\overline{\Phi}_I$ is the $2N_{II} \times 2N_I$ fixed-interface complex modal matrix and Λ_I is the corresponding $2N_I \times 2N_I$ reduced diagonal eigenvalue matrix. For systems with mixed damping, $\overline{\Phi}_I$ can be partitioned into a matrix $\overline{\Phi}_{IU}$ collecting $2N_U$ underdamped eigenvectors and another matrix $\overline{\Phi}_{IO}$ collecting $2N_O$ overdamped eigenvectors. Together, $\overline{\Phi}_{IU}$ and $\overline{\Phi}_{IO}$ contain eigenvectors up to the $2N_I$ th mode, such that $2N_I = 2N_U + 2N_O$. The matrices $\overline{\Phi}_I$ and Λ_I can be explicitly written as follows

$$\overline{\Phi}_{I} = \begin{bmatrix} \overline{\Phi}_{IU} & \overline{\Phi}_{IO} \end{bmatrix} \text{ and } \Lambda_{I} = \operatorname{diag} [\lambda_{k}], \text{ with}
\overline{\Phi}_{IU} = \begin{bmatrix} \overline{\mathbf{y}}_{IU}^{1} & \overline{\mathbf{y}}_{IU}^{2} & \cdots & \overline{\mathbf{y}}_{IU}^{2N_{U}} \end{bmatrix} \text{ and } \overline{\Phi}_{IO} = \begin{bmatrix} \overline{\mathbf{y}}_{IO}^{1} & \overline{\mathbf{y}}_{IO}^{2} & \cdots & \overline{\mathbf{y}}_{IO}^{2N_{O}} \end{bmatrix}$$
(20)

where $k=1,2,\ldots,2N_{\rm I},\,\lambda_k$ is the kth eigenvalue, $\overline{\bf y}_{\rm IU}^n$ $(n=1,2\ldots,2N_{\rm U})$ is the nth eigenvector of $\overline{\bf \Phi}_{\rm IU}$ and $\overline{\bf y}_{\rm IO}^m$ $(m=1,2\ldots,2N_{\rm O})$ is the mth eigenvector of $\overline{\bf \Phi}_{\rm IO}$. It should be noted that the complex modal matrix $\overline{\bf \Phi}_{\rm I}$ in its unstructured form (as directly obtained from Eq. (19)) may degrade the numerical stability and computational performance of the remaining steps in the reduction process. To circumvent this problem, Boukadia et al. suggested that a modified reduction basis composed by the separation of the real and imaginary parts of $\overline{\bf \Phi}_{\rm IU}$ should be used instead of $\overline{\bf \Phi}_{\rm I}$ [64]. The modified complex modal matrix reads

$$\overline{\overline{\Phi}}_{I} = \begin{bmatrix} \mathbf{Re} \left(\overline{\Phi}_{IU} \right) & \mathbf{Im} \left(\overline{\Phi}_{IU} \right) & \overline{\Phi}_{IO} \end{bmatrix}$$
 (21)

where the number of columns of $\overline{\Phi}_{IU}$ has been doubled, shifting from $\overline{\Phi}_I$ to $\overline{\overline{\Phi}}_I$. Next, a Singular Value Decomposition (SVD) of the modified reduction basis is performed to avoid the possibility of further numerical instabilities that may arise due to the presence of redundant vectors in $\overline{\overline{\Phi}}_I$. The outcome from such SVD leads to a factorization of the form

$$\overline{\overline{\Phi}}_{I} = \mathbf{U}^{T} \mathbf{\Sigma} \mathbf{V} \tag{22}$$

where U and V are complex unitary matrices containing the left and right singular vectors of $\overline{\overline{\Phi}}_I$, respectively, and Σ is a rectangular diagonal matrix with non-negative singular values in its diagonals. The final complex modal

matrix $\widehat{\Phi}_I$ is built by gathering the left singular vectors corresponding to the p largest singular values, where p is dependent on the accuracy and computational cost desired [37]. Once $\widehat{\Phi}_I$ is obtained, we can proceed by deriving a set of constraint modes in the augmented state variable space. To this end, the fixed-interface state vector \mathbf{y}_I can be written as follows

$$\mathbf{y}_{\mathbf{I}}(t) = \begin{cases} \mathbf{u}_{\mathbf{I}}(t) \\ \dot{\mathbf{u}}_{\mathbf{I}}(t) \end{cases} = \begin{bmatrix} \mathbf{\Psi} & \mathbf{0} \\ \mathbf{0} & \mathbf{\Psi} \end{bmatrix} \begin{cases} \mathbf{u}_{\mathbf{A}}(t) \\ \dot{\mathbf{u}}_{\mathbf{A}}(t) \end{cases} + \begin{bmatrix} \widehat{\mathbf{\Phi}}_{\eta\eta} & \widehat{\mathbf{\Phi}}_{\eta\dot{\eta}} \\ \widehat{\mathbf{\Phi}}_{\dot{\eta}\eta} & \widehat{\mathbf{\Phi}}_{\dot{\eta}\dot{\eta}} \end{bmatrix} \begin{cases} \boldsymbol{\eta}_{\mathbf{I}}(t) \\ \dot{\boldsymbol{\eta}}_{\mathbf{I}}(t) \end{cases}$$
(23)

where $\widehat{\Phi}_{\eta\eta}$, $\widehat{\Phi}_{\eta\dot{\eta}}$, $\widehat{\Phi}_{\dot{\eta}\eta}$, and $\widehat{\Phi}_{\dot{\eta}\dot{\eta}}$ are partitions of the complex modal matrix $\widehat{\Phi}_{\rm I}$. It should be noted that the same relations between the internal and interface displacements and velocities are used in both Eqs. (14) and (23). Conversely, the physical and modal internal displacements and velocities are not coupled to each other in Eq. (14), whereas such coupling is present in Eq. (23) since the complex modal matrix $\widehat{\Phi}_{\rm I}$ is fully populated. The total state vector can therefore be approximated using the following transformation of coordinates

$$\mathbf{y}(t) = \begin{cases} \mathbf{y}_{\mathrm{I}}(t) \\ \mathbf{y}_{\mathrm{A}}(t) \end{cases} = \begin{cases} \mathbf{u}_{\mathrm{I}}(t) \\ \dot{\mathbf{u}}_{\mathrm{I}}(t) \\ \mathbf{u}_{\mathrm{A}}(t) \\ \dot{\mathbf{u}}_{\mathrm{A}}(t) \end{cases} = \begin{bmatrix} \widehat{\mathbf{\Phi}}_{\eta\eta} & \widehat{\mathbf{\Phi}}_{\eta\dot{\eta}} & \mathbf{\Psi} & \mathbf{0} \\ \widehat{\mathbf{\Phi}}_{\dot{\eta}\eta} & \widehat{\mathbf{\Phi}}_{\dot{\eta}\dot{\eta}} & \mathbf{0} & \mathbf{\Psi} \\ \mathbf{0} & \mathbf{0} & \mathbf{I} & \mathbf{0} \\ \mathbf{0} & \mathbf{0} & \mathbf{0} & \mathbf{I} \end{bmatrix} \begin{cases} \boldsymbol{\eta}_{\mathrm{I}}(t) \\ \dot{\boldsymbol{\eta}}_{\mathrm{I}}(t) \\ \mathbf{u}_{\mathrm{A}}(t) \\ \dot{\mathbf{u}}_{\mathrm{A}}(t) \end{cases}$$
(24)

which can also be written in the following compact form

$$\mathbf{y}(t) = \begin{cases} \mathbf{y}_{\mathrm{I}}(t) \\ \mathbf{y}_{\mathrm{A}}(t) \end{cases} = \underbrace{\begin{bmatrix} \widehat{\Phi}_{\mathrm{I}} & \widehat{\Psi} \\ \mathbf{0} & \widehat{\mathbf{I}} \end{bmatrix}}_{\mathbf{T}_{\mathrm{CO}}} \underbrace{\begin{cases} \mathbf{h}_{\mathrm{I}}(t) \\ \mathbf{y}_{\mathrm{A}}(t) \end{cases}}_{\mathbf{y}_{\mathrm{A}}(t)}$$
(25)

where T_{SS} is referred to as the state-space transformation matrix, and

$$\mathbf{h}_{\mathbf{I}}(t) = \begin{cases} \boldsymbol{\eta}_{\mathbf{I}}(t) \\ \dot{\boldsymbol{\eta}}_{\mathbf{I}}(t) \end{cases}, \quad \widehat{\boldsymbol{\Phi}}_{\mathbf{I}} = \begin{bmatrix} \widehat{\boldsymbol{\Phi}}_{\eta\eta} & \widehat{\boldsymbol{\Phi}}_{\eta\dot{\eta}} \\ \widehat{\boldsymbol{\Phi}}_{\dot{\eta}\eta} & \widehat{\boldsymbol{\Phi}}_{\dot{\eta}\dot{\eta}} \end{bmatrix}, \quad \widehat{\boldsymbol{\Psi}} = \begin{bmatrix} \boldsymbol{\Psi} & \mathbf{0} \\ \mathbf{0} & \boldsymbol{\Psi} \end{bmatrix}, \quad \widehat{\mathbf{I}} = \begin{bmatrix} \mathbf{I} & \mathbf{0} \\ \mathbf{0} & \mathbf{I} \end{bmatrix}$$
(26)

Substituting Eq. (25) into Eq. (16) and pre-multiplying Eq. (16) by T_{SS}^{T} , the equations of motion governing the reduced-order model become

$$A\dot{\mathbf{y}}_{\mathbf{r}}(t) + B\mathbf{y}_{\mathbf{r}}(t) = \mathbf{0} \tag{27}$$

where

$$A = \mathbf{T}_{SS}^{T} \mathbf{A} \mathbf{T}_{SS}$$
 and $B = \mathbf{T}_{SS}^{T} \mathbf{B} \mathbf{T}_{SS}$ (28)

are the reduced state-space matrices and \mathbf{y}_r is the reduced free state vector. Finally, appropriate Bloch periodicity boundary conditions need to be enforced to compute the desired band structures. As stated earlier, the Bloch periodicity boundary conditions derived in Section 2 for full-order systems can be easily extended to classically damped reduced-order systems. Unfortunately, this is not the case for non-classically damped reduced-order systems. The main reason behind this limitation is that the size of the Bloch periodicity matrix \mathbf{P} in its common form as in Eq. (4) is not compatible with the size of the state-space matrices \mathbf{A} and \mathbf{B} . A modified and expanded version of the Bloch periodicity matrix that is suitable for reduced state-space models is therefore needed. To this end, we initially assume plane harmonic waves of the form $\mathbf{y}_r(t) = \overline{\mathbf{y}}_r \exp(\lambda t)$. Substituting the previous equation into Eq. (27) yields $(\lambda \mathbf{A} + \mathbf{B}) \overline{\mathbf{y}}_r = \mathbf{0}$, where $\overline{\mathbf{y}}_r = \{\overline{\mathbf{h}}_1^T \ \overline{\mathbf{y}}_A^T\}^T = \{\overline{\mathbf{\eta}}_{1,u}^T \ \overline{\mathbf{\eta}}_{1,v}^T \ \overline{\mathbf{u}}_{A,u}^T \ \overline{\mathbf{u}}_{A,v}^T \}^T$ and for consistency with the analysis in Section 2, $\overline{\mathbf{u}}_{A,u}$ and $\overline{\mathbf{u}}_{A,v}$ are partitioned according to Eq. (2). Next, a set of Bloch periodicity boundary conditions are enforced using the following augmented state variable space format

$$\left\{ \begin{array}{c} \overline{\eta}_{I,u} \\ \overline{\eta}_{I,v} \\ \overline{u}_{A,u} \\ \overline{v}_{r} \end{array} \right\} = \underbrace{\begin{bmatrix} \mathbf{I}_{I} & \mathbf{0} & \mathbf{0} & \mathbf{0} \\ \mathbf{0} & \mathbf{I}_{I} & \mathbf{0} & \mathbf{0} \\ \mathbf{0} & \mathbf{0} & \mathbf{P}_{A} & \mathbf{0} \\ \mathbf{0} & \mathbf{0} & \mathbf{0} & \mathbf{P}_{A} \end{bmatrix}}_{\mathbf{P}_{SS}} \underbrace{\begin{bmatrix} \tilde{\eta}_{I,u} \\ \tilde{\eta}_{I,v} \\ \tilde{u}_{A,u} \\ \tilde{u}_{A,v} \\ \tilde{y}_{I} \end{array}}_{\tilde{y}_{I}} \tag{29}$$

where P_{SS} is the augmented state-space Bloch periodicity matrix and

$$\mathbf{P}_{A}(\mathbf{\kappa}) = \begin{bmatrix} \mathbf{I}_{L} & \mathbf{0} & \mathbf{0} \\ \alpha_{1}\mathbf{I}_{R} & \mathbf{0} & \mathbf{0} \\ \mathbf{0} & \mathbf{I}_{B} & \mathbf{0} \\ \mathbf{0} & \alpha_{2}\mathbf{I}_{T} & \mathbf{0} \\ \mathbf{0} & \mathbf{0} & \mathbf{I}_{LB} \\ \mathbf{0} & \mathbf{0} & \alpha_{1}\mathbf{I}_{RB} \\ \mathbf{0} & \mathbf{0} & \alpha_{2}\mathbf{I}_{LT} \\ \mathbf{0} & \mathbf{0} & \alpha_{1}\alpha_{2}\mathbf{I}_{RT} \end{bmatrix}$$
(30)

is denoted as the interface Bloch periodicity matrix, which is slightly different from Eq. (4). With Eq. (29) in hand, the eigenvalue problem

$$\left[\lambda(\kappa)\widetilde{A}(\kappa) + \widetilde{B}(\kappa)\right]\widetilde{\mathbf{y}}_{r}(\kappa) = \mathbf{0} \tag{31}$$

with $\widetilde{A} = \mathbf{P}_{SS}^H \mathbf{A} \, \mathbf{P}_{SS}$ and $\widetilde{\mathbf{B}} = \mathbf{P}_{SS}^H \mathbf{B} \, \mathbf{P}_{SS}$, is sufficient to compute the desired band structures of the reduced-order model. We will denote the proposed method SS-BMS, for state-space BMS.

4. Application and performance evaluation of the SS-BMS method

In this section, we evaluate the computational performance of the proposed reduction method using two applications of periodic materials. The first application represents a typical example of a phononic crystal. It consists of a 2D plate that is comprised of two material phases with different densities, elastic moduli, and damping properties (see Fig. 2a). In the second application, a damped locally resonant metamaterial is studied—a benchmark example that has been repeatedly seen in the literature (see Fig. 2b). In both applications, 4-noded non-conforming rectangular plate elements are used to develop the finite-element mesh, with each node having five DOFs to describe the middle surface transverse displacement, the two bending rotations, and the two shear rotations of the plate about its planar coordinates. This finite element follows the Mindlin plate theory assumptions. Moreover, it has been proven to exhibit good convergence for linear systems [65]. All computations are implemented in Matlab 2018b using a standard personal computer.

4.1. Problem I: Phononic crystal

The first periodic material and its representative square-shaped unit cell that we use to evaluate the proposed method are shown in Fig. 2a. The unit cell is comprised of a silicone rubber (Sil) matrix housing an aluminum (Al) inclusion, thus resembling a commonly investigated form of phononic crystals. It is assumed that the aluminum inclusion is embedded into the silicone rubber matrix through an open cut rather than attaching the inclusion to the surface of the matrix. The lattice constant of the unit cell is a = 0.02 m and its thickness is h = 0.002 m. The material properties are given as follows: aluminum with mass density $\rho_{A1} = 2799 \,\mathrm{Kg/m^3}$, Young's modulus $E_{\rm Al} = 72.1$ GPa, and Poisson's ratio $\nu_{\rm Al} = 0.3$ and silicone rubber with mass density $\rho_{\rm Sil} = 1300\,{\rm Kg/m^3}$, Young's modulus $E_{Sil} = 118 \,\mathrm{kPa}$, and Poisson's ratio $v_{Sil} = 0.468$. The frequency band structure of this unit cell in its undamped configuration has been already produced in a previous work [66], enabling us to verify the results for this particular example. Non-classical dissipation is realized by assuming that material phases contribute to the overall damping behavior differently, which means that each material phase has its own specific damping characteristics. Without loss of generality, proportional damping models of the form $\mathbf{D}_{A1} = \alpha_{A1}\mathbf{K}_{Sil}$ and $\mathbf{D}_{Sil} = \alpha_{Sil}\mathbf{K}_{Sil}$ are used to describe the damping behavior in both phases, where \mathbf{K}_{Sil} is the stiffness matrix associated with silicone rubber, while \mathbf{D}_{Al} and \mathbf{D}_{Sil} are the damping matrices associated with aluminum and silicone rubber, respectively. With the above models, the amount of prescribed damping in each phase can be controlled by varying its corresponding proportionality constant (α_{Al} for aluminum and α_{Sil} for silicone rubber). Initially, it is beneficial to test a range of proportionality constants before proceeding into the computational analysis. To this end, Fig. 3 shows three

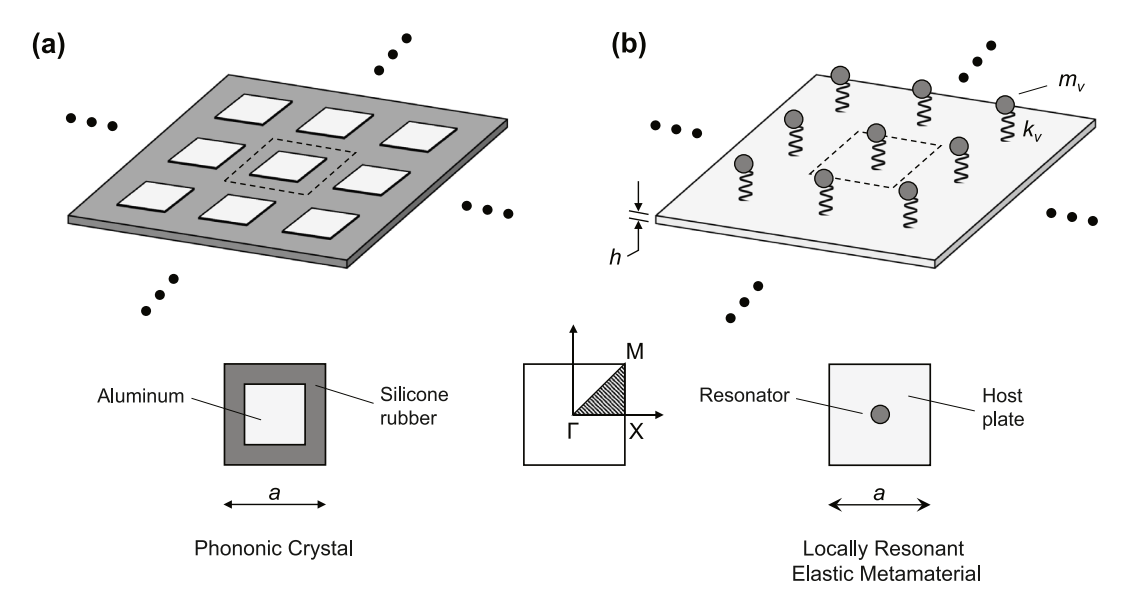


Fig. 2. Schematic of the investigated (a) phononic crystal and (b) locally resonant elastic metamaterial, along with their representative unit cells.

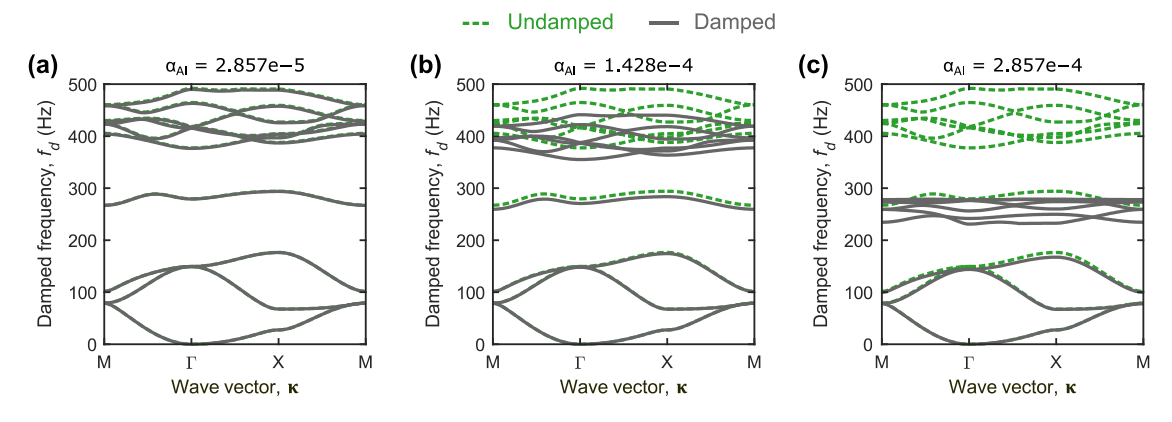


Fig. 3. Phononic crystal: A preliminary test showing frequency band structures corresponding to three different prescribed damping levels. For simplicity, it is assumed that $\alpha_{Sil} = 2\alpha_{Al}$ so that band-structure evolution can be depicted as function of α_{Al} only. The first ten dispersion branches of the damped unit cells are plotted using gray-solid lines while their counterparts corresponding to the undamped case are plotted using green-dotted lines. (For interpretation of the references to color in this figure legend, the reader is referred to the web version of this article.)

frequency band structures corresponding to three different prescribed damping levels (plotted with gray-solid lines). For simplicity, $\alpha_{Sil} = 2\alpha_{Al}$ is selected for all three test cases so that the band-structure evolution can be depicted as function of α_{Al} only. The values $\alpha_{Al} = 2.857 \times 10^{-5}$ s/rad, $\alpha_{Al} = 1.428 \times 10^{-4}$ s/rad, and $\alpha_{Al} = 2.857 \times 10^{-4}$ s/rad are used to compute the band structures in Figs. 3a, 3b, and 3c, respectively. To clearly isolate the influence of increased prescribed damping on the results, the undamped unit-cell's frequency band structure is superimposed on all the figures (plotted with green-dotted lines). The results reveal that the damped frequency band structure corresponding to the smallest proportionality constant ($\alpha_{Al} = 2.857 \times 10^{-5}$ s/rad) is barely distinguishable from its undamped counterpart implying the unit cell is lightly damped in this particular case (see Fig. 3a). However, downward shifts of the dispersion frequencies (see Figs. 3b and 3c) become clearly noticeable as a result of increased prescribed damping levels, as expected. Consequently, the subsequent analysis in this section will be based on the second case (with $\alpha_{Al} = 1.428 \times 10^{-4}$ s/rad) for the following reasons: (1) unlike the first case (i.e., Fig. 3a), Fig. 3b represents a case where the frequency band structure is clearly altered by non-classical damping, (2) unlike the third case

Full order model

Reduced order model (50 underdamped modes) Reduced order model (50 underdamped + 100 overdamped modes) (a) 500 Close-up Damped frequency, f_{d} (Hz) Damped frequency, f_{σ} (Hz) 440 300 430 200 420 100 410 0 400 M Х к* M Х Wave vector, κ Wave vector, k (b) 0.45 Close-up 0. 0.44 Damping ratio, ζ Damping ratio, ζ 0.3 0.43 0.2 0.42 0.1 0.41 0 0.4 Γ Χ к* M M Χ Μ M Γ Wave vector, ĸ Wave vector, ĸ

Fig. 4. Phononic crystal: A comparison between the band structures of the full-order model (black-solid lines) and two different reduced-order models (orange-dashed and blue-dotted lines). The reduced models are comprised of reduction bases that are detailed in the legend. The left column of figures depicts the first ten dispersion branches corresponding to the (a) damped frequency and (b) damping ratio band structures and the right column of figures represent close-ups of (a) and (b), respectively. The dotted-vertical line along the κ^* -point in the left panel in (a) and (b) is needed for later analysis. (For interpretation of the references to color in this figure legend, the reader is referred to the web version of this article.)

(i.e., Fig. 3c), the bandgaps are not curtailed significantly, and (3) the proportionality constant $\alpha_{Al} = 1.428 \times 10^{-4}$ s/rad leads to a scenario of mixed damping, which is realistic in practice, especially for unit cells comprising rubber elements; this aspect will be discussed in detail shortly. Finally, we note that Fig. 3 displays only the first ten dispersion branches computed for 120 κ -points and without any reduction in the system size (i.e., using the full-order model) using a finite element mesh with a total of 2205 displacement DOFs in the free unit cell (4410 DOFs in the state-space).

With the dispersion curves of the full-order model in hand, the attention now is shifted towards the performance of the proposed reduction method. As a starting point, Fig. 4 shows a comparison between the band structures of the full-order model (plotted with black-solid lines) and two different reduced-order models (plotted with orange-dashed and blue-dotted lines), with a finite element mesh that is identical to the one used to produce Fig. 3. The first reduced model (orange-dashed) retains only 50 interior modes in its reduction basis while the second reduced model (blue-dotted) retains 150 interior modes. The full model unit-cell internal dynamics exhibit mixed damping with 2284 underdamped modes and 1326 overdamped modes. All of the 50 interior modes kept in the first reduced model are picked from the underdamped modes, which means that the 1326 overdamped modes are entirely excluded from the reduction basis in this model. In the second reduced model, however, the retained 150 interior modes comprise a combination of 50 underdamped modes and 100 overdamped modes. It is important to note that the reason behind selecting a mixed-mode reduction basis in the second reduced model (and the precise way of deciding

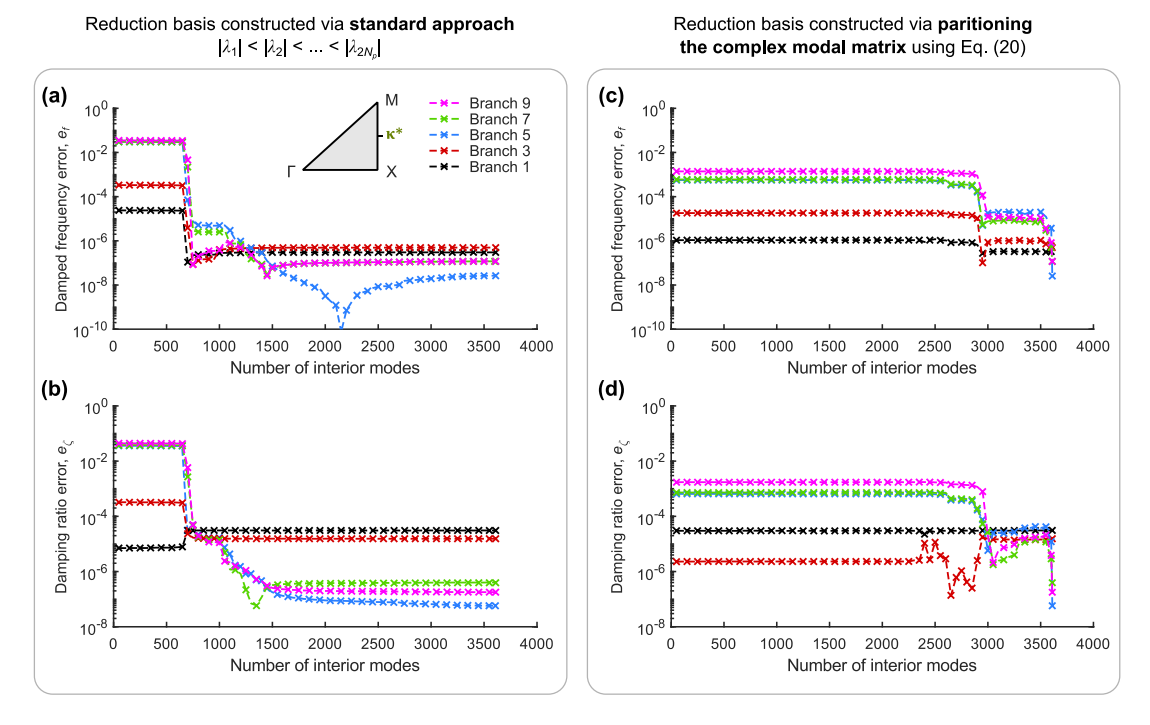


Fig. 5. Phononic crystal: Frequency and damping ratio errors computed for five points that correspond to the intersection of the dotted-vertical lines in Fig. 4 (at the κ^* -point) with the first (black), third (red), fifth (blue), seventh (green), and ninth (magenta) dispersion branches. In (a) and (b), the reduction basis is constructed using the standard approach in which the absolute values of the eigenvalues are organized in ascending order. In (c) and (d), the reduction basis is constructed by partitioning the underdamped and overdamped modes according to Eq. (20). (For interpretation of the references to color in this figure legend, the reader is referred to the web version of this article.)

on the modal composition) is not justified at this point because this requires careful analysis which will be detailed later in this section. While Fig. 4 shows that both reduced-order models are in very good visual agreement with the full-order model, the second reduced model (blue-dotted) produces more accurate results as can be seen clearly in the close-ups. However, more accurate comparisons between the reduced-order and full-order models can be achieved by calculating the following frequency and damping ratio relative errors

$$e_f = \left| \frac{\omega_{d,\text{red}} - \omega_{d,\text{full}}}{\omega_{d,\text{full}}} \right| \text{ and } e_{\zeta} = \left| \frac{\zeta_{\text{red}} - \zeta_{\text{full}}}{\zeta_{\text{full}}} \right|$$
 (32)

In what follows, we will dissect the problem using a series of steps which not only provides a more comprehensive understanding of the inner-workings of the state-space reduction method, but will also lead to important conclusions. As a first step, we will examine how the relative errors, defined in Eq. (32), evolve with the number of interior modes in the reduced-order model. To simplify the analysis, the errors will be computed for only one κ -point, but any conclusions drawn at this step will later be checked across the irreducible Brillouin zone (IBZ). The computed frequency and damping ratio errors are displayed in Fig. 5 for five points that correspond to the intersection of the dotted-vertical lines in Figs. 4a and 4b (at a κ -point, denoted κ^* -point, located precisely halfway through the X-M path in the IBZ) with the first (black), third (red), fifth (blue), seventh (green), and ninth (magenta) dispersion branches. In Figs. 5a and 5b, the errors are computed when the eigenvalues are ordered such that $|\lambda_1| < |\lambda_2| < \cdots < |\lambda_{2N_p}|$, with the corresponding eigenvectors following the same order, and the number of interior modes is increased by increments of 50 modes. The results show clearly that as the number of interior modes is increased, the solution displays a convergent behavior as expected. It should be noted that while the approach used here in ordering the eigenvalues and the corresponding eigenvectors is standard (i.e., identical to the approach used to tackle undamped systems), it is not unique. To justify this point, let us examine where the underdamped and overdamped eigenvalues (of the fixed-interface unit cell) are located if their absolute values are organized in ascending order. This is shown in Fig. 6a, which plots the absolute values of the underdamped eigenvalues (green)

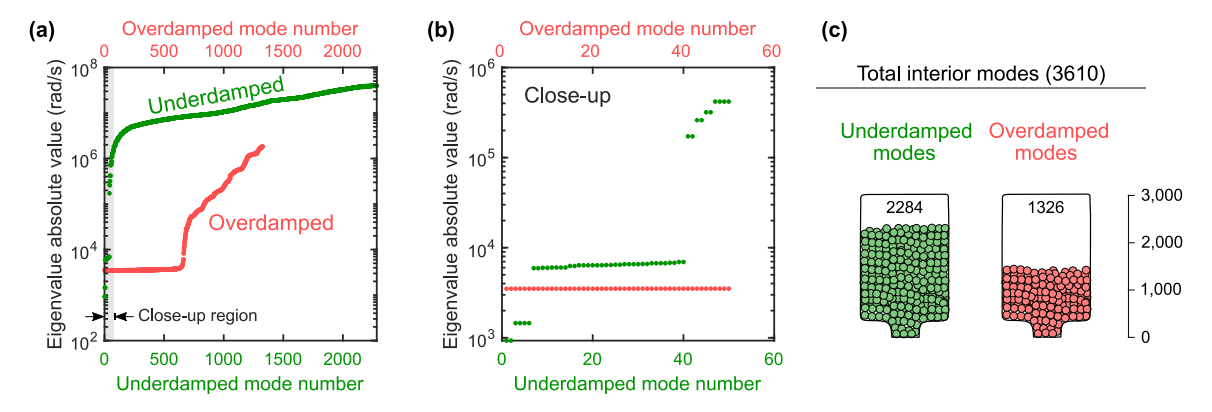


Fig. 6. Phononic crystal: (a) Absolute values of the 2284 underdamped eigenvalues (green) and the 1326 overdamped eigenvalues (red) corresponding to the fixed-interface state-space eigenvalue problem. The plot in (b) represents a close-up of (a), showing only the first 50 underdamped modes and the first 50 overdamped modes. In (c), the two sets of underdamped and overdamped modes are partitioned in two separate "containers"—a simple visualization approach that will shortly prove its worth in the illustration of two different mode-selection schemes. (For interpretation of the references to color in this figure legend, the reader is referred to the web version of this article.)

and the overdamped eigenvalues (red), superimposed on top of each other. Moreover, Fig. 6b provides a close-up of Fig. 6a, showing only the first 50 underdamped modes and the first 50 overdamped modes. From Fig. 6, we conclude that the underdamped modes are not separated from the overdamped modes if the standard ordering approach (discussed previously) is used to construct the reduction basis (which is used to compute the errors in Figs. 5a and 5b). Consequently, a different approach for computing the errors involves partitioning the complex modal matrix according to Eq. (20). The errors computed using this approach are shown in Figs. 5c and 5d. Compared with the standard ordering approach, partitioning the complex modal matrix provides the following advantages: (1) it leads to a faster convergence rate which can be seen when Figs. 5c and 5d are compared to Figs. 5a and 5b, respectively. For example, when only 50 interior modes are used in the reduced models, an order of magnitude improvement (or greater) is achieved for all the five data points in Fig. 5, and (2) it provides a convenient platform by which the effects of underdamped modes as well as the effects of overdamped modes can be studied individually or in combined form. We highlight that while the underdamped modes are known to dominate the system response in the oscillatory frequency range, the contribution of overdamped modes to the system's response (and the accuracy of dispersion curves) is not trivial in the high damping regime, as will be shown next.

To demonstrate how both the underdamped and overdamped modes can influence the accuracy of dispersion curves, errors at the κ^* -point are further dissected in Fig. 7. Fig. 7a displays the evolution of errors when the reduction basis of the reduced-order model is comprised of underdamped modes only. Computation of the errors in Fig. 7a is executed in two steps: (1) In the first step, the number of underdamped interior modes is increased from 2 to 50. At this step, the errors decrease with the increase of the number of modes as expected (except for the point on the first damping ratio dispersion branch which shows a non-monotonic, yet converging error behavior). However, the extent of such decrease in the errors is not consistent between the different points. For example, when 50 interior modes are used, relative errors corresponding to the points on the first and third branches (with lower frequencies and lower damping ratios) are significantly smaller than relative errors of the remaining points on the higher dispersion branches. Nevertheless, the maximum errors are within an order of 10^{-3} when 50 underdamped modes are incorporated. (2) In the second step, the errors are computed when the number of underdamped interior modes is increased from 50 to 2284. Intriguingly, Fig. 7a reveals that when the number of underdamped modes is increased beyond 50, no improvements in the errors are gained.

Next, Fig. 7b depicts the errors when the first 50 underdamped modes are augmented with 50 to 1326 overdamped modes to form the reduction basis. The results reveal that significant frequency and damping ratio error improvements are achieved when overdamped modes are included in the reduction basis. However, more than half the total number of overdamped modes (around 700 modes) is needed to achieve noticeable error improvements. This is attributed to the fact that companion pairs of overdamped modes start to build up in the reduced-order model only after passing through the halfway point along the *x*-axes in Fig. 7b plot. It should be noted that while

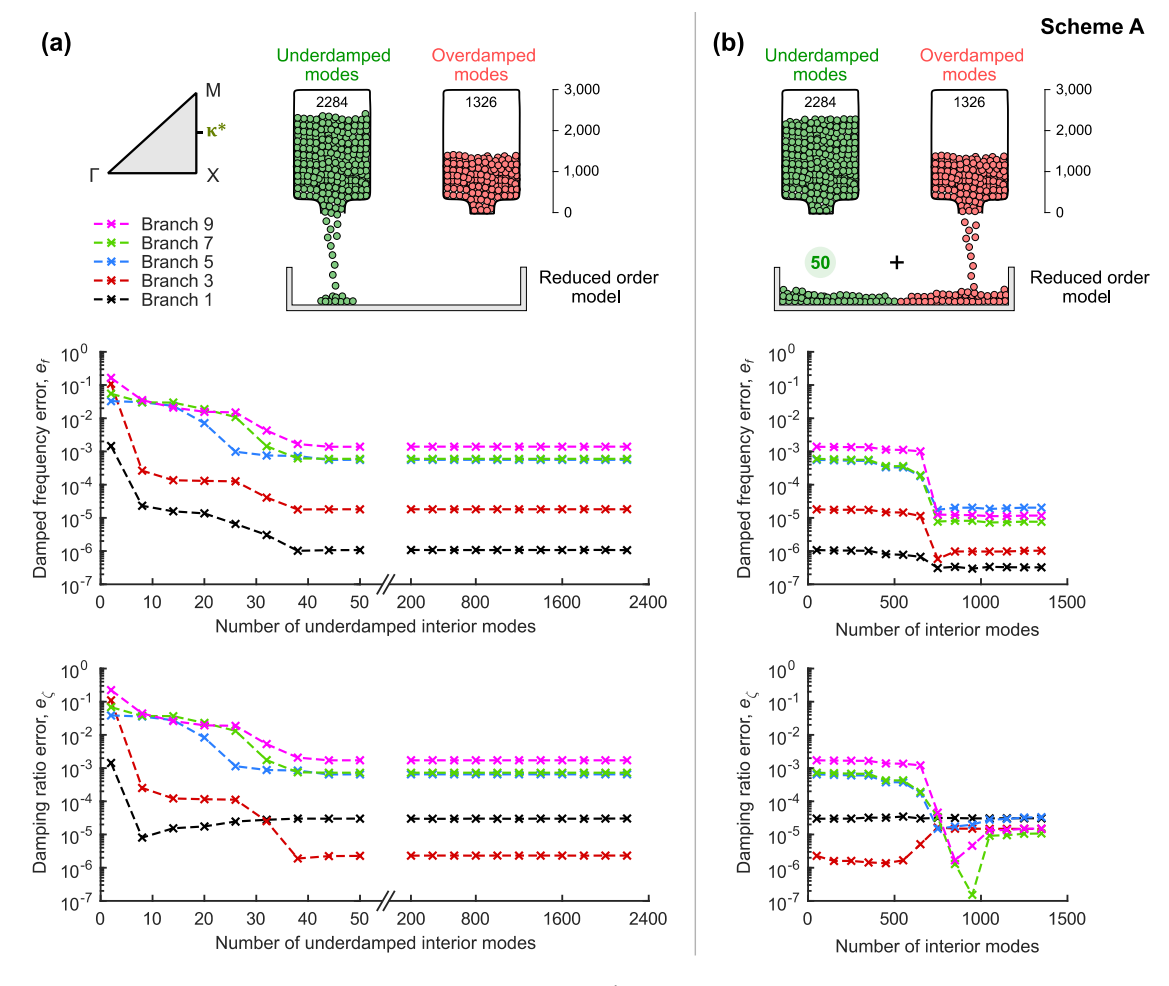


Fig. 7. Phononic crystal: Frequency and damping ratio errors at the κ^* -point using Scheme A: The plots in (a) display the evolution of errors when the number of interior modes is increased using a reduction basis comprised of underdamped modes only, and the plots in (b) display the evolution of errors when the number of interior modes is increased using a reduction basis comprised of mixed-modes (with fixed 50 underdamped modes but increasing number of overdamped modes). The approach used in (b) is what we denote as Scheme A.

the presented scheme (denoted here as *Scheme A*) is straightforward to implement, it is counterproductive when the number of overdamped modes becomes extremely large as it curtails the ability to speed-up the band-structure computations.

The previous analysis suggests that more efficient reduced-order models can potentially be built if the overdamped modes are ordered in companion pairs, rather than ordering them in terms of their absolute values. However, this hypothesis is yet to be validated. To this end, *Scheme B* is proposed, which is based on the idea of using a reduction basis that is comprised of 50 underdamped modes in combination with a selected group (or groups) of 50 companion pairs of overdamped modes (i.e., 100 overdamped modes). Knowing that the unit-cell internal modal model exhibits a total of 1326 overdamped modes, this is equivalent to 663 companion mode pairs. We now divide the overdamped mode pairs into groups, with each group collecting only 50 pairs. This means that the first group collects the first 50 mode pairs, the second group collects the second 50 mode pairs, and so forth. By following this mode assembly exercise, we end up with 14 groups of companion mode pairs. Here, we must note that Group 14 (i.e., the last group) collects the last 50 mode pairs (i.e., the last 100 overdamped modes) of the 663 companion mode pairs. Next, the frequency and damping ratio relative errors are computed at the κ^* -point, as shown in Fig. 8, for the 14 reduced-order models in hand. The goal here is to search for the most dominant group of companion mode pairs that produces the most accurate results. It is observed from Fig. 8 that the greatest error reduction is attained when

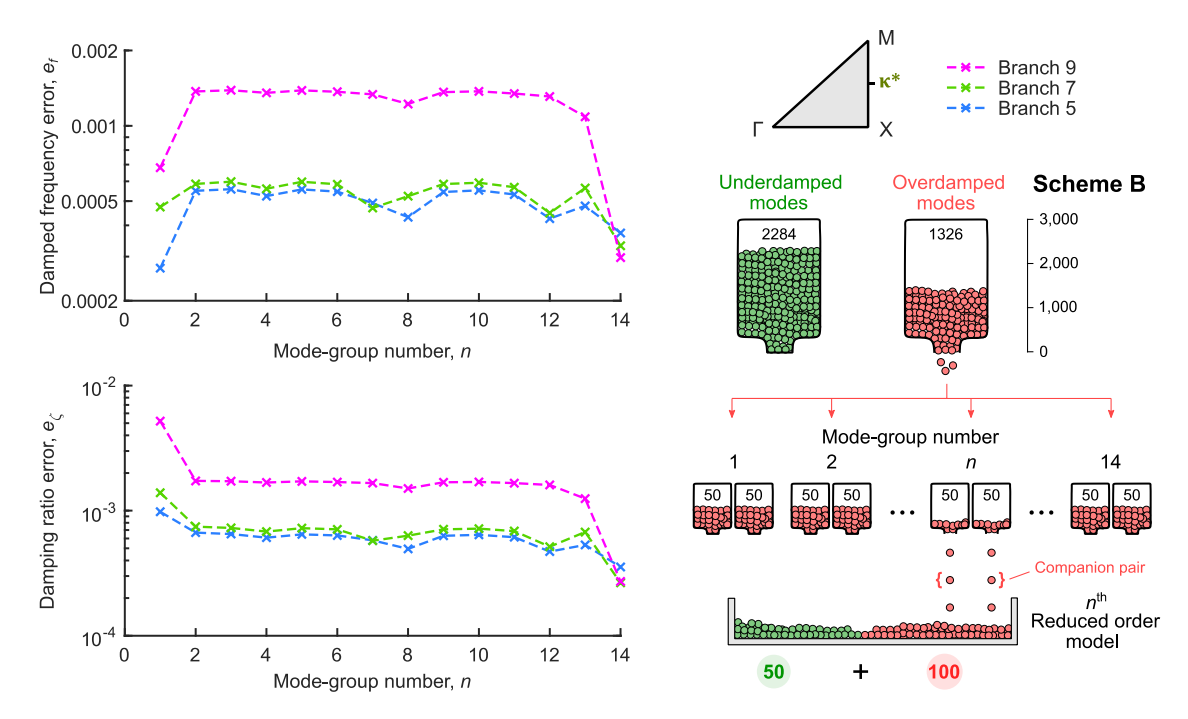


Fig. 8. Phononic crystal: Frequency and damping ratio errors at the κ^* -point using Scheme B: The errors are computed using 14 different reduced-order models. First, the 1326 overdamped modes are divided into 14 groups of companion pairs with each group collecting 50 companion mode pairs (i.e., 100 overdamped modes). The reduction basis of the *n*th reduced-order model is comprised of 50 underdamped modes in combination with the *n*th group of 50 companion pairs of overdamped modes (i.e., a total of 150 modes).

the last group of companion pairs is used in the reduced-order model, which is another intriguing behavior. Finally, we highlight that searching for the most dominant overdamped modes is considered an intermediate step which manifests itself as a drawback of Scheme B when compared to Scheme A. In terms of model sizes, however, the 150-modes reduced model obtained using Scheme B is superior to the 750-modes reduced model obtained using Scheme A.

The observations drawn thus far (using both Schemes A and B) are based on results obtained at one κ -point. It is therefore important to validate these observations across the IBZ. In Fig. 9, the frequency and damping ratio errors are compared for three different reduced-order models (first: black-solid, second: orange-dashed, third: bluedotted). In the first model, the reduction basis is composed of 50 underdamped modes only, the second model is obtained using Scheme A (with 750 modes), which we will refer to as a Scheme A realization, while the third model is obtained using Scheme B (with 150 modes), which we will refer to as a Scheme B realization. For better visualization, the errors corresponding to the first frequency and damping ratio dispersion branches are shown separately in Fig. 9a. Similarly, the errors corresponding to the second and third dispersion branches are shown in Fig. 9b, while the errors corresponding to the remaining branches (branches 4 through 10) are shown in Fig. 9c. It can be seen that apart from the first dispersion branch, the maximum relative errors are: (1) within acceptable limits for the first model but (2) are significantly improved using the second and third models. In particular, Fig. 9c reveals that when the first model is utilized, the maximum errors are in the order of 10^{-3} while they are in the order of 10⁻⁴ when the second (or third) model is utilized. On the other hand, due to the extremely small values of the solutions attained in the vicinity of the singularity point Γ , Fig. 9a reveals that the maximum relative errors are around 4%-5% for the first frequency and damping ratio dispersion branches. It should be noted that rather than being modeling errors, these are likely round-off errors or ill-conditioning errors that may arise from the existence of simultaneously very large and very small eigenvalues [67]. Fortunately, eigensolutions obtained in the proximity region around Γ are typically not of practical significance in most structural dynamics applications. For example, the maximum damping ratio relative error in Fig. 9a is about $e_{\zeta} = 4.7\%$. The corresponding damping ratios of the reduced-order and full-order models are $\zeta_{\rm red} = 6.04 \times 10^{-7}$ and $\zeta_{\rm full} = 1.14 \times 10^{-6}$, respectively. Despite

Computational costs calculated for Scheme A realization vs. Scheme B realization; both used to plot Fig. 9.					
Step	Scheme A realization	Scheme B realization	Full-order model		
State-space model size: before applying Bloch BCs (after applying Bloch BCs)	1550 DOFs (1140 DOFs)	950 DOFs (540 DOFs)	4410 DOFs (4000 DOFs)		
Up-front time Time per one κ -point Total time (120 κ -points)	$t_{\text{red}}^{\text{up}} = 12.38 \text{ s}$ $t_{\text{red}}^{\kappa} = 1.11 \text{ s}$ $t_{\text{red}} = 2 \text{ m } 26 \text{ s}$	$t_{\text{red}}^{\text{up}} = 12.38 \text{ s}$ $t_{\text{red}}^{\mathbf{k}} = 0.22 \text{ s}$ $t_{\text{red}} = 38.78 \text{ s}$	NA $t_{\text{full}}^{\mathbf{k}} = 21.93 \text{ s}$ $t_{\text{full}} = 43 \text{ m } 52 \text{ s}$		

Table 1
Computational costs calculated for Scheme A realization vs. Scheme B realization; both used to plot Fig. 9

the relatively high relative error obtained in this case, the absolute difference between ζ_{red} and ζ_{full} is trivial from a practical standpoint. Consequently, the absolute error provides a more sensible measure in this case as the difference between the two damping ratios is in the order of 10^{-7} . Finally, Fig. 9a shows that as we move away from the proximity region around Γ , the first frequency and damping ratio dispersion branches produce extremely small relative errors as expected. From the previous analysis, we conclude that the inclusion of overdamped modes is only recommended when high accuracy results are required in the high damping regime.

Finally, as usually done with model reduction schemes, critical assessment of the performance should be based also on comparing the times needed to compute the band structures of the reduced-order and full-order models, denoted as t_{red} and t_{full} , respectively, where

$$t_{\text{red}} = n_{\kappa} \times t_{\text{red}}^{\kappa} + t_{\text{red}}^{\text{up}} \quad \text{and} \quad t_{\text{full}} = n_{\kappa} \times t_{\text{full}}^{\kappa}$$
 (33)

where n_{κ} denotes the total number of κ -points used in the band-structure computations, t_{red}^{κ} and t_{full}^{κ} are, respectively, the times required to compute the reduced model and full model solutions at one κ -point, and $t_{\text{red}}^{\text{up}}$ is the up-front time needed to perform the reduction itself. Table 1 summarizes the computational costs of the reduced-order models obtained from Schemes A and B; used to plot Fig. 9 (i.e., Scheme A realization vs. Scheme B realization).

4.2. Problem II: Locally resonant elastic metamaterial

In the second test problem, the SS-BMS method is applied to a damped locally resonant elastic metamaterial (see Fig. 2b). A representative unit cell consists of plate with a local resonator attached. The host plate has a mass density $\rho = 2700 \, \text{Kg/m}^3$, a Young's modulus $E = 70 \, \text{GPa}$, and a Poisson's ratio v = 0.3. The local resonator has a damping ratio $\zeta_v = 0.1$ and is tuned to a natural frequency $f_v = (1/2\pi)\sqrt{k_v/m_v} = 1.5 \, \text{kHz}$ with $m_v = 0.2m_p$, where m_p is the mass of the host plate in a single cell. The unit cell with a lattice constant $a = 0.04 \, \text{m}$ and thickness $h = 0.002 \, \text{m}$ is discretized with a finite element mesh identical to the one used in the first test problem. Moreover, proportional damping of the form $\mathbf{D} = \alpha \mathbf{K}$ is used for the host plate, where \mathbf{D} and \mathbf{K} are the corresponding damping and stiffness matrices and $\alpha = 5.71 \times 10^{-6} \, \text{s/rad}$. For this example, the unit-cell internal modal model exhibits mixed damping with 16 underdamped modes and 3594 overdamped modes.

Fig. 10 shows a comparison between the band structures of the full-order model (plotted with black-solid lines) and two different reduced-order models (plotted with orange-dashed and blue-dotted lines). The first reduced model (orange-dashed) retains only all of its 16 underdamped modes in its reduction basis while the second reduced model (blue-dotted) retains a combination of all 16 underdamped modes plus 300 overdamped modes (i.e., a total of 316 interior modes). We note that the precise way of deciding on the modes to be incorporated in the second reduced model will be clarified shortly. It is clear from Fig. 10 that the second reduced model (blue-dotted) is more accurate than the first (orange-dashed), especially in the high damping regime.

The influence of both the underdamped modes and the overdamped modes on the errors at the κ^* -point is displayed in Fig. 11. In Fig. 11a, the evolution of errors is shown when the number of interior modes is increased from 2 to 16 underdamped modes only, whereas Fig. 11b depicts the errors when the 16 underdamped modes are augmented with 200 to 3200 overdamped modes to form the reduction basis. From Fig. 11a, it can be seen that the errors decrease with the increase of underdamped modes, as expected. However, the extent of such decrease in the errors is not the same between the different points-an observation that has also been seen in the first example (phononic crystal). Because only underdamped modes are used to construct Fig. 11a, the maximum errors are

Reduced order model: 50 underdamped modes only
 Reduced order model: Scheme A realization (50 underdamped + 700 overdamped modes = 750 modes)
 Reduced order model: Scheme B realization (50 underdamped + 100 overdamped modes* = 150 modes)
 *Last mode-group of overdamped companion modes = {50 x 2} = 100

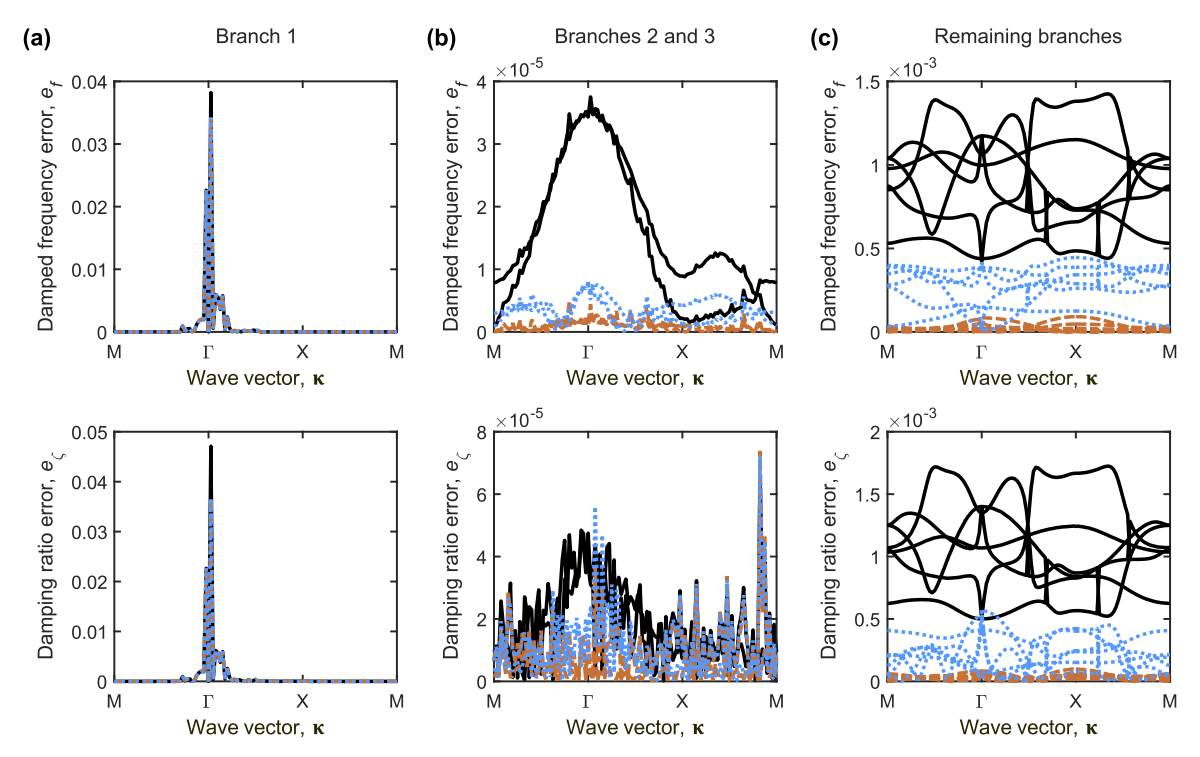


Fig. 9. Phononic crystal: Frequency and damping ratio errors, computed across the IBZ for three different reduced-order models. The reduced models are comprised of reduction bases that are detailed in the legend. The leftmost column of figures depicts the errors corresponding to the first dispersion branch. The middle column shows the errors corresponding to the second and third dispersion branches, and the rightmost column displays the errors corresponding to the remaining branches (branches 4 through 10).

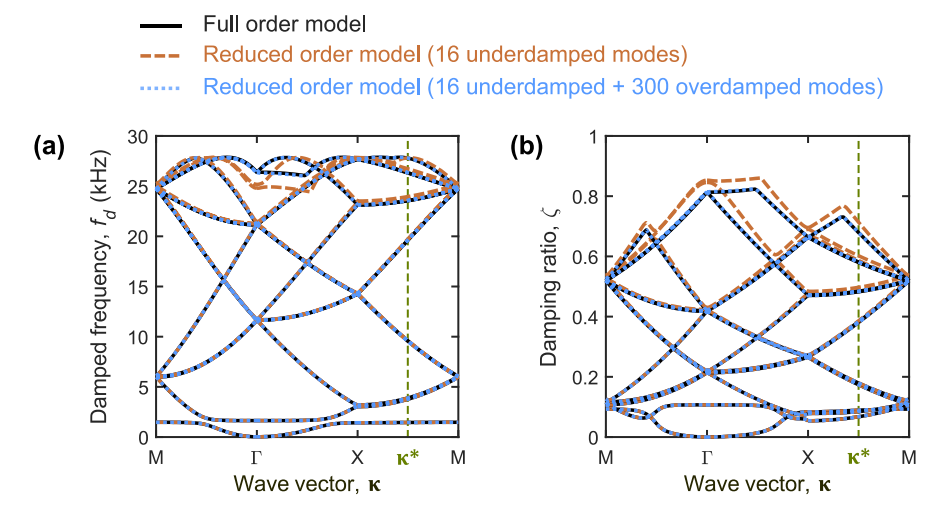


Fig. 10. Elastic metamaterial: A comparison between the band structures of the full-order model (black-solid lines) and two different reduced-order models (orange-dashed and blue-dotted lines). The reduced models are comprised of reduction bases that are detailed in the legend. The plot in (a) depicts the first twelve damped frequency dispersion branches while the plot (b) shows the first twelve damping ratio dispersion branches. Moreover, the κ^* -point is marked in (a) and (b) for later analysis. (For interpretation of the references to color in this figure legend, the reader is referred to the web version of this article.)

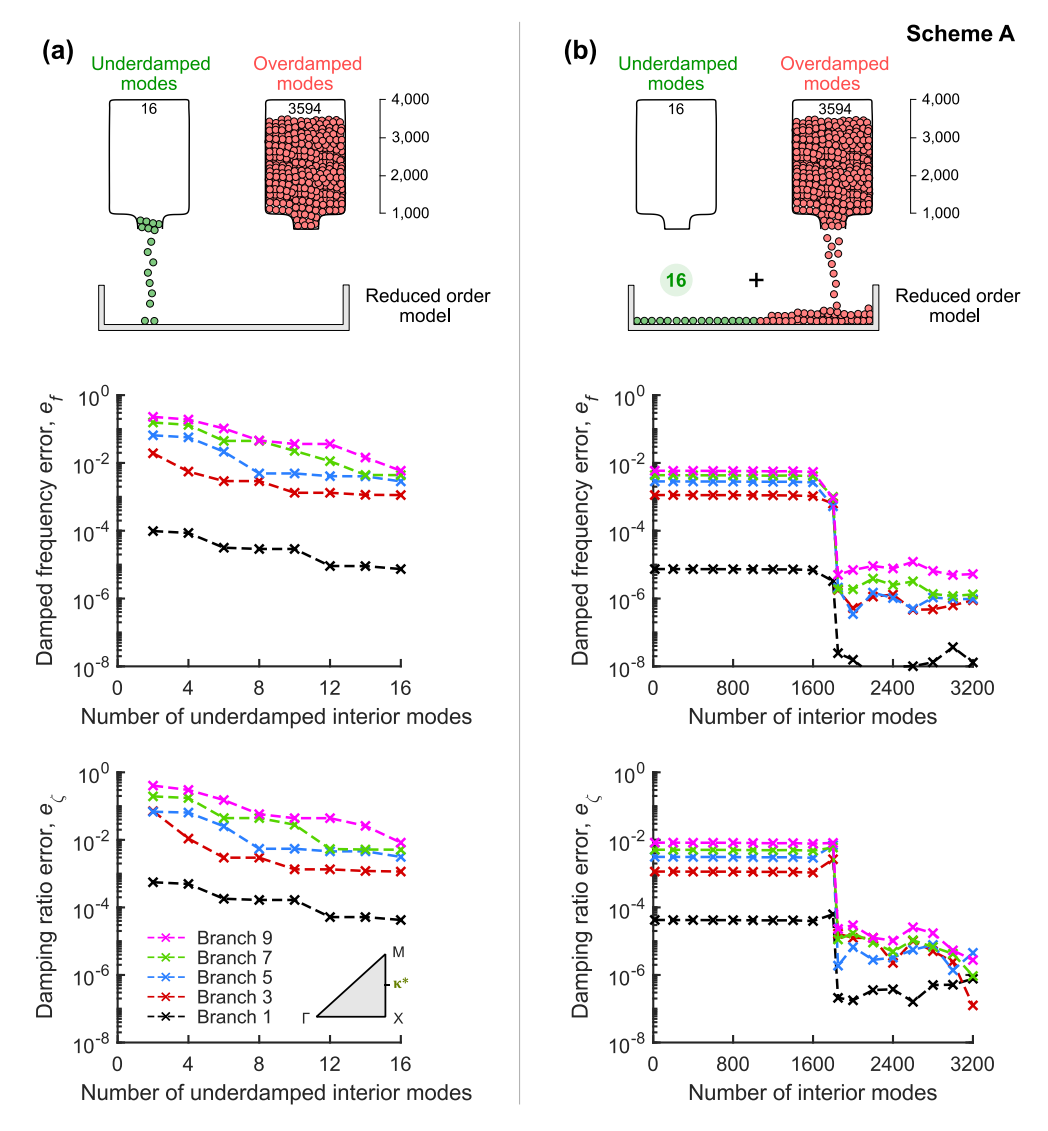


Fig. 11. Elastic metamaterial: Frequency and damping ratio errors at the κ^* -point using Scheme A: The plots in (a) display the evolution of errors when the number of interior modes is increased using a reduction basis comprised of underdamped modes only, and the plots in (b) displays the evolution of errors when the number of interior modes is increased using a reduction basis comprised of mixed-modes (with fixed 16 underdamped modes but increasing number of overdamped modes).

found to be relatively high, even when all the 16 underdamped modes are taken into account. However, significant frequency and damping ratio error improvements are achieved when overdamped modes are included in the reduction basis as inferred from Fig. 11b. Once again, by using Scheme A, more than half the total number of overdamped modes (around 1835 modes in this case) is needed to achieve error improvements, which is counterproductive.

To circumvent the poor computational efficiency of Scheme A, attention is switched to Scheme B which utilizes overdamped modes in companion pairs. The reduction basis in Scheme B is comprised of 16 underdamped modes in combination with a selected group (or groups) of 50 companion pairs of overdamped modes. Knowing that the unit-cell internal dynamics exhibit a total of 3594 overdamped modes, this is equivalent to 1797 companion mode pairs. By dividing the companion overdamped modes into groups of 50 pairs, we end up with 36 groups. Then, the frequency and damping ratio relative errors are computed at the **k***-point (see Fig. 12), for the 36 reduced-order models in hand. While Fig. 12 reveals that the greatest error reduction is attained when the last group of companion pairs is used in the reduced-order model, it is clear that the first group is also influencing the errors.

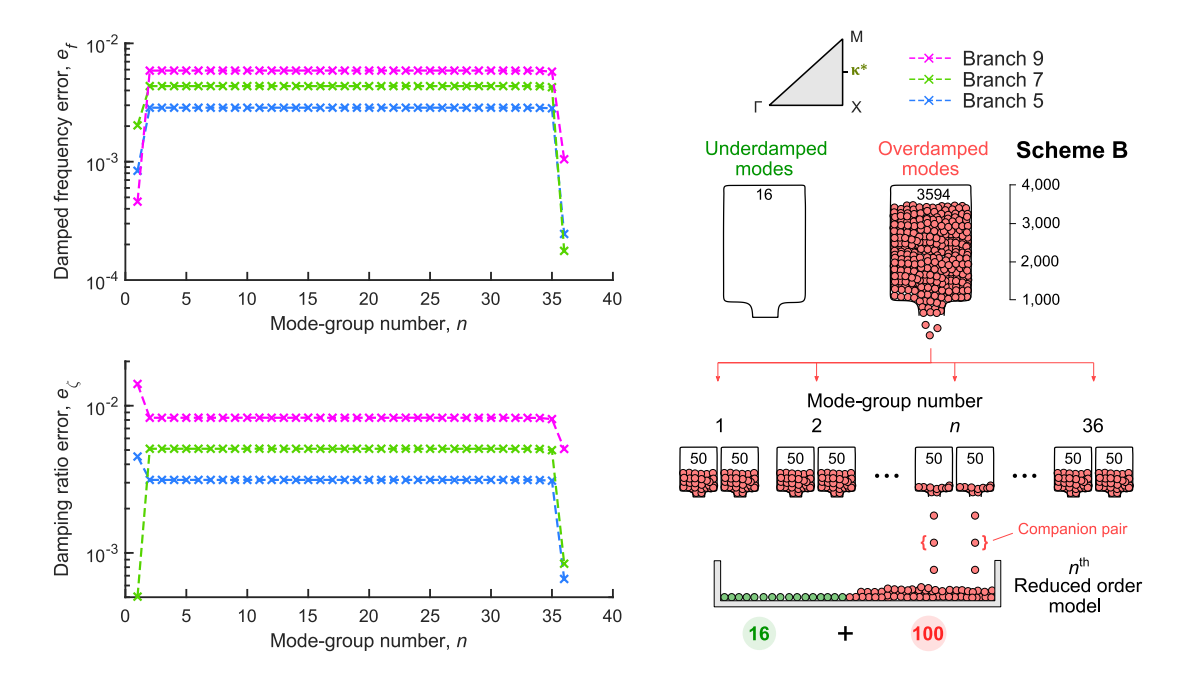


Fig. 12. Elastic metamaterial: Frequency and damping ratio errors at the κ^* -point using Scheme B: The errors are computed using 36 reduced-order models. First, the 3594 overdamped modes are divided into 36 groups of companion pairs with each group collecting 50 companion mode pairs (i.e., 100 overdamped modes). The reduction basis of the *n*th reduced-order model is comprised of 16 underdamped modes in combination with the *n*th group of 50 companion pairs of overdamped modes (i.e., a total of 116 modes).

Therefore, instead of computing the IBZ errors using only one realization of Scheme B (as we did in the previous test problem), we compare the errors obtained from three different realizations of Scheme B. While the reduction bases used in all the three realizations contain 16 underdamped modes, they are augmented with different groups of companion overdamped mode pairs as follows: (1) In the first of these realizations, only the last group of 50 companion mode pairs are used, (2) in the second, the first two groups of 50 companion mode pairs are used, and (3) in the third, the companion mode pairs used in the prior realizations are combined together. Fig. 13 shows a comparison between the errors computed using these three Scheme B realizations (first realization: black-solid, second realization: orange-dashed, third realization: blue-dotted). For brevity, the errors are computed only for the fifth dispersion branch (leftmost column), the seventh dispersion branch (middle column), and the ninth branch (rightmost column). It is clear that the third realization produces the most accurate results, especially in the high damping regime.

Finally, Fig. 14 compares the frequency and damping ratio errors for three different reduced-order models (first: black-solid, second: orange-dashed, third: blue-dotted). In the first model, the reduction basis is composed of 16 underdamped modes only, the second model is identical to the Scheme A realization (with 1850 modes), while the third model is identical to the third Schemes B realization (with 316 modes). For better visualization, the errors corresponding to the first frequency and damping ratio dispersion branches are shown separately in Fig. 14a. The errors corresponding to the second through the fifth dispersion branches are shown in Fig. 14b, while the errors corresponding to the remaining branches (branches 6 through 10) are shown in Fig. 14c. It can be seen that the first reduced model produces relatively high errors. However, the second and third models provide significant error improvements. Moreover, the third model (third realization of Scheme B) is considered the best choice because it is the most efficient among the three models. We finally provide Table 2 which summarizes the computational costs of Scheme A realization vs. third realization of Scheme B.

- Reduced order model: Scheme B 1st realization
 (16 underdamped modes + last mode-group of overdamped companion modes)
- Reduced order model: Scheme B 2nd realization
 (16 undamperdamped modes + first two mode-groups of overdamped companion modes)
- Reduced order model: Scheme B 3rd realization
 (16 underdamped modes + first two and last mode-groups of overdamped companion modes)

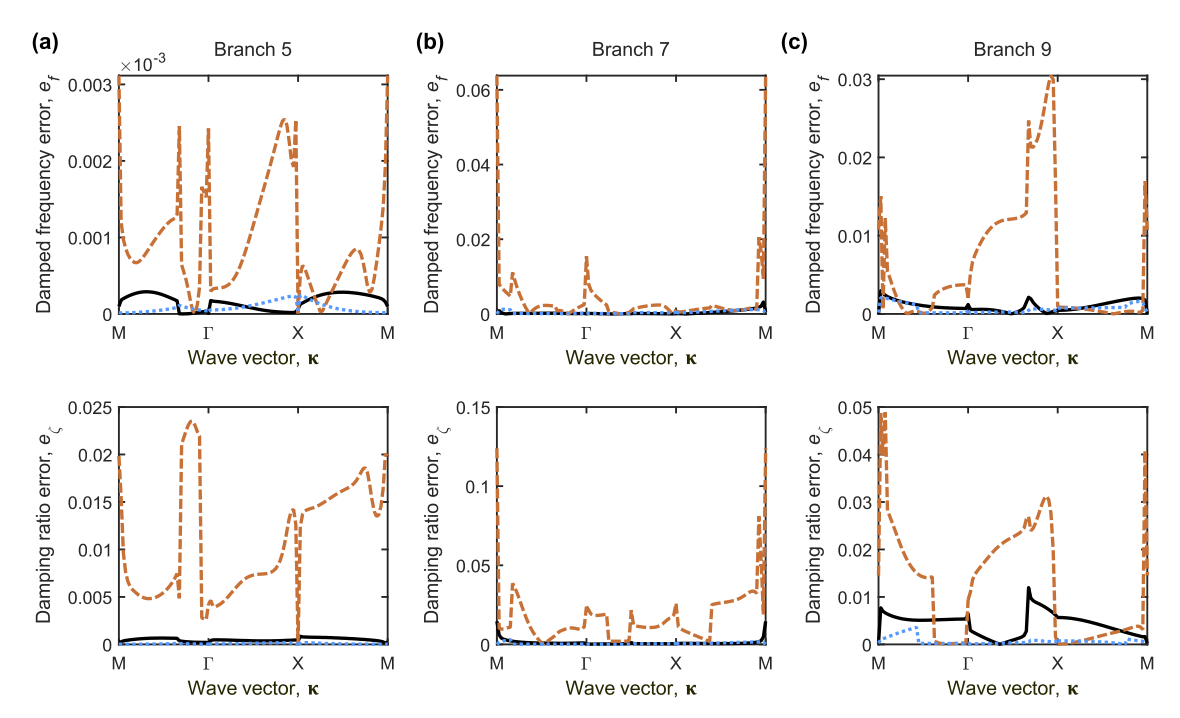


Fig. 13. Elastic metamaterial: Frequency and damping ratio errors, computed across the IBZ using the first, second, and third Scheme B realizations. The three realizations are comprised of reduction bases that are detailed in the legend. Note that the first realization utilizes 116 modes, while the second and third realizations contain 216 modes and 316 modes, respectively. The leftmost column of figures depicts the errors corresponding to the fifth dispersion branch. The middle column shows the errors corresponding to the seventh dispersion branch, and the rightmost column displays the errors corresponding to the ninth dispersion branch.

Table 2
Computational costs calculated for Scheme A realization vs. Scheme B third realization; both used to plot Fig. 14.

Step	Scheme A realization	Scheme B 3rd realization	Full-order model
State-space model size: before applying Bloch BCs (after applying Bloch BCs)	2650 DOFs (2240 DOFs)	1116 DOFs (706 DOFs)	4412 DOFs (4002 DOFs)
Up-front time Time per one κ -point Total time (120 κ -points)	$t_{\text{red}}^{\text{up}} = 12.38 \text{ s}$ $t_{\text{red}}^{\text{K}} = 5.49 \text{ s}$ $t_{\text{red}} = 11 \text{ m } 11 \text{ s}$	$t_{\text{red}}^{\text{up}} = 12.38 \text{ s}$ $t_{\text{red}}^{\text{K}} = 0.39 \text{ s}$ $t_{\text{red}} = 59.18 \text{ s}$	NA $t_{\text{full}}^{\kappa} = 21.99 \text{ s}$ $t_{\text{full}} = 43 \text{ m} 59 \text{ s}$

4.3. Error-computation time performance maps

We conclude our performance analysis with Fig. 15, which displays an overall performance map relating the maximum damped frequency and damping ratio errors (e_f^{\max} and e_{ζ}^{\max} , respectively) to the computation time ($t_{\text{red}}/t_{\text{full}}$). The maps show numerous discrete points with circle markers. Each point in each of the subplots is representative of a unique reduced-order model. The maximum errors are computed across the IBZ for branches 2 through 9 only (first branch is excluded from the computations to avoid the unbounded solution at the singularity

Wave vector, ĸ

Wave vector, κ

Reduced order model: 16 underdamped modes only --- Reduced order model: Scheme A realization (16 underdamped + 1834 overdamped modes = 1850 modes) Reduced order model: Scheme B 3rd realization (16 underdamped + 300 overdamped modes* = 316 modes) *First two mode-groups of overdamped companion modes = 2 x {50 x 2} = 200, and last mode-group of overdamped companion modes = {50 x 2} = 100 (a) (b) (c) Branches 2-5 Branch 1 Remaining branches _10⁻³ × 10⁻⁴ 0.02 Damped frequency error, $e_{_{\it f}}$ e, a, Damped frequency error, Damped frequency error, 0.015 0.0 0.5 0.005 Χ М Г М M M Wave vector, κ Wave vector, κ Wave vector, κ ×10⁻⁴ 0.03 Damping ratio error, $e_{_{ \subset}}$ Damping ratio error, $e_{_{\zeta}}$ Damping ratio error, $\boldsymbol{e}_{_{\!\mathcal{C}}}$ 0.02 0.0 0 0 n Х М M M Г Х М Х M M

Fig. 14. Elastic metamaterial: Frequency and damping ratio errors, computed across the IBZ for three different reduced-order models. The reduced models are comprised of reduction bases that are detailed in the legend. The leftmost column of figures depicts the errors corresponding to the first dispersion branch. The middle column shows the errors corresponding to the second through fifth dispersion branches, and the rightmost column displays the errors corresponding to the remaining branches (branches 6 through 10).

Wave vector, κ

point Γ and the relatively large errors in the region surrounding Γ). In Figs. 15a and 15b, the errors are displayed for the first test problem (phononic crystal) while Figs. 15c and 15d depict the errors for the second test problem (locally resonant elastic metamaterial). In both test problems, all the discrete points are computed using reduced-order models that comprise a combination of underdamped modes and overdamped modes. The number of underdamped modes used in the reduction basis is fixed at 50 for the phononic crystal (i.e., in Figs. 15a and 15b) while it is fixed at 16 for the locally resonant elastic metamaterial (i.e., in Figs. 15c and 15d). The data points are divided into four categories that are distinguished using four different colors. Each color represents a specific approach for augmenting the overdamped modes into the reduced-order model. More specifically, the four colors match the following selection approaches: (see Supplementary Materials for the actual numerical values for the data points):

- Black points are used when overdamped modes are augmented into the reduced-order model with the absolute values of their eigenvalues being organized in ascending order, i.e., Scheme A. The overdamped modes are not augmented as companion pairs in this case.
- Red points are used when overdamped modes are augmented into the reduced-order model as companion pairs, i.e., Scheme B. Specifically, the absolute values of λ_m (and λ_{m+N_0}) in Eq. (9) are organized in ascending order.
- Blue points are used when overdamped modes are augmented into the reduced-order model as companion pairs, i.e., Scheme B. Specifically, the absolute values of λ_m (and λ_{m+N_0}) in Eq. (9) are organized in descending order
- Green points are used when arbitrarily selected combinations of overdamped companion modes are augmented into the reduced-order model.

From all four performance maps provided, it is clear that any of the black, red, or blue sets provide, at the extreme, a case with minimum computation time; only the error is observed to be least for the blue group among

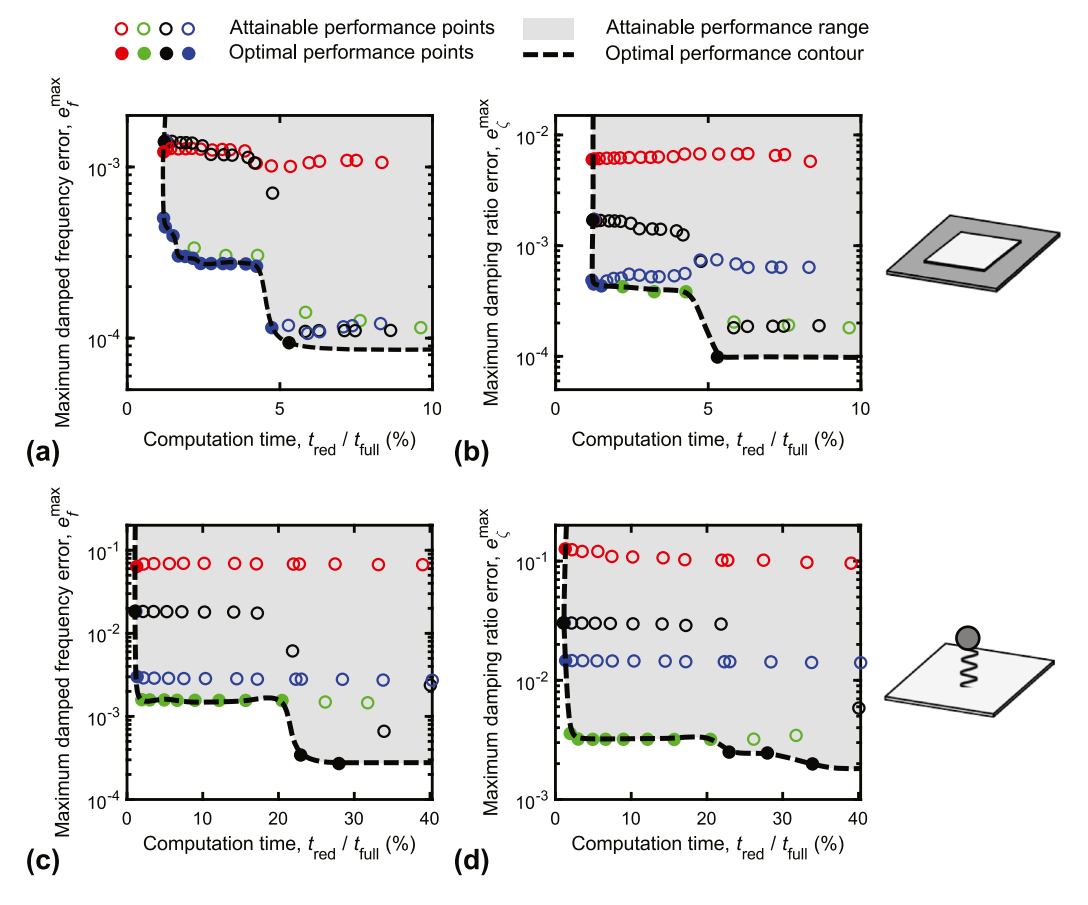


Fig. 15. Phononic crystal and elastic metamaterial: Performance plot of maximum (a) frequency and (b) damping ratio error versus computation time for phononic crystal model, and performance plot of maximum (c) frequency and (d) damping ratio error versus computation time for elastic metamaterial model. Color code for the data points is described in the text.

these three sets. Further reduction in error is achieved by the green set, which also demonstrates extreme cases that give excellent computation times. This colored composition of the reduced-order models demonstrates how the specific selection of the overdamped modes plays a profound role in determining the performance. Frontier lines are drawn to trace the border along the bottom-left edge of each performance region, which indicate how far the proposed SS-BMS method can reach towards the ideal performance spot at the far bottom-left corner of each plot.

5. Conclusions

We provided a state-space generalization of the BMS fast band-structure computation method to allow for the treatment of non-classical damping in the unit-cell model. The new method is denoted SS-BMS. Due to the general complexity of non-classical damping, a relatively moderate level of prescribed damping produces an eigensolution that comprises a combination of underdamped and overdamped modes, appearing in complex form. Furthermore, these modes do not line up as two separate groups when the absolute value of the eigenvalues is plotted versus mode number; they instead mix in their line up as shown in Fig. 6. A monotonic mode selection process is therefore no longer optimal, in contrast to the cases of undamped or classically damped models. To address this issue, we have proposed two mode-selection schemes for the reduction of the unit-cell internal model. In both schemes, a certain number of underdamped modes is selected and augmented with a certain number of overdamped modes. In Scheme A, the overdamped modes are ordered according to the absolute value of the eigenvalues, and are selected monotonically. In Scheme B, the overdamped modes are collected as companion pairs and ordered as such, forming sets of mode-groups.

We examined the performance of both scheme classes on two examples of plate-based problems, a phononic crystal with a relatively large number of underdamped modes and a locally resonant elastic metamaterial with a relatively small number of underdamped modes. Band structures computed from reduced-order models constructed based on both schemes are shown to provide excellent agreement with their counterparts obtained from the full-order model. In Scheme A, noticeable error improvements are attained when more than half of the overdamped modes are augmented into the reduced-order model, after which the addition of further overdamped modes yields insignificant improvements. Well selected realizations of Scheme B provide a good balance between accuracy and computational speed.

The presented results demonstrate how overdamped modes play a significant role in the construction of reducedorder models, even when the focus is on obtaining dispersion curves associated with only underdamped traveling waves. An error-computation time trade-off for each scheme will guide the practitioner on which scheme to use depending on needs for the specific problem being analyzed. This investigation does not only extend the applicability of BMS techniques to the most generally damped models of periodic media, it also advances our understanding of the nature of damping modes and the non-trivial manner by which they contribute to the wave propagation properties, including both frequencies and damping ratios.

Declaration of competing interest

The authors declare that they have no known competing financial interests or personal relationships that could have appeared to influence the work reported in this paper.

Appendix A. Supplementary data

Supplementary material related to this article can be found online at https://doi.org/10.1016/j.cma.2022.115018.

References

- [1] M.I. Hussein, M.J. Leamy, M. Ruzzene, Dynamics of phononic materials and structures: historical origins, recent progress, and future outlook, Appl. Mech. Rev. 66 (2014) 40802.
- [2] Y. Jin, Y. Pennec, B. Bonello, H. Honarvar, L. Dobrzynski, B. Djafari-Rouhani, M.I. Hussein, Physics of surface vibrational resonances: pillared phononic crystals, metamaterials, and metasurfaces, Rep. Progr. Phys. 84 (2021) 086502.
- [3] F. Bloch, Über die quantenmechanik der elektronen in kristallgittern, Z. Phys. 52 (1928) 555-600.
- [4] O. Sigmund, J.S. Jensen, Systematic design of phononic band-gap materials and structures by topology optimization, Philos. Trans. R. Soc. A 361 (2003) 1001–1019.
- [5] A.S. Phani, J. Woodhouse, N.A. Fleck, Wave propagation in two-dimensional periodic lattices, J. Acoust. Soc. Am. 119 (2006) 1995–2005.
- [6] M.I. Hussein, Reduced Bloch mode expansion for periodic media band structure calculations, Proc. R. Soc. Lond. Ser. A Math. Phys. Eng. Sci. 465 (2009) 2825–2848.
- [7] B.R. Mace, D. Duhamel, M.J.J. Brennan, Finite element prediction of wave motion in structural waveguides, J. Acoust. Soc. Am. 117 (2005) 2835–2843.
- [8] B.R. Mace, E. Manconi, Modelling wave propagation in two-dimensional structures using finite element analysis, J. Sound Vib. 318 (2008) 884–902.
- [9] M.I. Hussein, Theory of damped Bloch waves in elastic media, Phys. Rev. B 80 (2009) 212301.
- [10] M.I. Hussein, M.J. Frazier, Band structure of phononic crystals with general damping, J. Appl. Phys. 108 (2010) 93506.
- [11] M.I. Hussein, M.J. Frazier, Metadamping: An emergent phenomenon in dissipative metamaterials, J. Sound Vib. 332 (2013) 4767–4774.
- [12] M.J. Frazier, M.I. Hussein, Generalized Bloch's theorem for viscous metamaterials: dispersion and effective properties based on frequencies and wave numbers that are simultaneously complex, C.R. Phys. 17 (2016) 565–577.
- [13] C.L. Bacquet, H. Al Ba'ba'a, M.J. Frazier, M. Nouh, M.I. Hussein, Metadamping: Dissipation emergence in elastic metamaterials, Adv. Appl. Mech. 51 (2018) 115–164.
- [14] A. Aladwani, M. Nouh, Mechanics of metadamping in flexural dissipative metamaterials: analysis and design in frequency and time domains, Int. J. Mech. Sci. 173 (2020) 105459.
- [15] A. Aladwani, M. Nouh, Strategic damping placement in viscoelastic bandgap structures: dissecting the metadamping phenomenon in multiresonator metamaterials, J. Appl. Mech. 88 (2021) 021003.
- [16] A. Aladwani, A. Mohammed, M. Nouh, Tunable dissipation in elastic metamaterials via methodic reconfiguration of inertant mechanical networks, Meccanica 57 (2022) 1337–1352.
- [17] R.P. Moiseyenko, V. Laude, Material loss influence on the complex band structure and group velocity in phononic crystals, Phys. Rev. B 83 (6) (2011) 064301.
- [18] M. Collet, M. Ouisse, M. Ruzzene, M. Ichchou, Floquet–Bloch decomposition for the computation of dispersion of two-dimensional periodic, damped mechanical systems, Int. J. Solids Struct. 48 (2011) 2837–2848.

- [19] T.K. Caughey, M.E.J. O'Kelly, Classical normal modes in damped linear dynamic systems, J. Appl. Mech. 32 (1965) 583-588.
- [20] J.W. Rayleigh, The Theory of Sound, Vol. 1, Dover, New York, 1894.
- [21] K.A. Foss, Co-ordinates which uncouple the equations of motion of damped linear dynamic systems, J. Appl. Mech. 25 (1958) 361-364.
- [22] A.S. Veletsos, C.E. Ventura, Modal analysis of non-classically damped linear systems, Earthq. Eng. Struct. Dyn. 14 (1986) 217–243.
- [23] A. Ibrahimbegovic, E.L. Wilson, Simple numerical algorithms for the mode superposition analysis of linear structural systems with non-proportional damping, Comput. Struct. 33 (1989) 523–531.
- [24] A.S. Phani, M.I. Hussein, Analysis of damped Bloch waves by the Rayleigh perturbation method, J. Vib. Acoust. 135 (2013) 041014.
- [25] M.I. Hussein, M.J. Frazier, M.H. Abedinnasab, Chapter 1: Microdynamics of phononic materials, in: Shaofan Li, Xinlin Gao (Eds.), Handbook of Micromechanics and Nanomechanics, Pan Stanford Publishing Co. Singapore, 2013, pp. 1–28.
- [26] P. Wang, L. Lu, K. Bertoldi, Topological phononic crystals with one-way elastic edge waves, Phys. Rev. Lett. 115 (2015) 104302.
- [27] R.K. Pal, M. Ruzzene, Edge waves in plates with resonators: An elastic analogue of the quantum valley hall effect, New J. Phys. 19 (2017) 025001.
- [28] P. Deymier, K. Runge, Sound Topology, Duality, Coherence and Wave-Mixing, Springer Nature, Cham, 2017.
- [29] X. Zhang, M. Xiao, Y. Cheng, M.-H. Lu, J. Christensen, Topological sound, Commun. Phys. 1 (2018) 97.
- [30] H. Al Ba'ba'a, M. Nouh, T. Singh, Dispersion and topological characteristics of permutative polyatomic phononic crystals, Proc. R. Soc. Lond. Ser. A Math. Phys. Eng. Sci. 475 (2019) 20190022.
- [31] O.R. Bilal, M.I. Hussein, Ultrawide phononic band gap for combined in-plane and out-of-plane waves, Phys. Rev. E 84 (2011) 065701.
- [32] Y. Lu, Y. Yang, J.K. Guest, A. Srivastava, 3-D phononic crystals with ultra-wide band gaps, Sci. Rep. 7 (2017) 1-14.
- [33] Z. Chen, A. Ogren, C. Daraio, L.C. Brinson, C. Rudin, How to see hidden patterns in metamaterials with interpretable machine learning, 2021, arXiv:2111.05949.
- [34] Y. Lu, A. Srivastava, Level repulsion and band sorting in phononic crystals, J. Mech. Phys. Solids 111 (2018) 100-112.
- [35] E.L. Shirley, Self-consistent GW and higher-order calculations of electron states in metals, Phys. Rev. B 54 (1996) 7758.
- [36] M.I. Hussein, G.M. Hulbert, Mode-enriched dispersion models of periodic materials within a multiscale mixed finite element framework, Finite Elem. Anal. Des. 42 (2006) 602–612.
- [37] A. Palermo, A. Marzani, A reduced Bloch operator finite element method for fast calculation of elastic complex band structures, Int. J. Solids Struct. 191–192 (2020) 601–613.
- [38] W.C. Hurty, Dynamic analysis of structural systems using component modes, AIAA J. 3 (1965) 678-685.
- [39] R.R. Craig JR., M.C.C. Bampton, Coupling of substructures for dynamic analyses, AIAA J. 6 (1968) 1313–1319.
- [40] V. Cotoni, R.S. Langley, P.J. Shorter, A statistical energy analysis subsystem formulation using finite element and periodic structure theory, J. Sound Vib. 318 (2008) 1077–1108.
- [41] D. Krattiger, M.I. Hussein, Bloch mode synthesis: Ultrafast methodology for elastic band-structure calculations, Phys. Rev. E 90 (2014) 63306
- [42] C. Zhou, J.-P. Lainé, M. Ichchou, A. Zine, Multi-scale modelling for two-dimensional periodic structures using a combined mode/wave based approach, Comput. Struct. 154 (2015) 145–162.
- [43] A. Palermo, A. Marzani, Extended Bloch mode synthesis: Ultrafast method for the computation of complex band structures in phononic media, Int. J. Solids Struct. 100–101 (2016) 29–40.
- [44] D. Krattiger, M.I. Hussein, Generalized Bloch mode synthesis for accelerated calculation of elastic band structures, J. Comput. Phys. 357 (2018) 183–205.
- [45] C. Xi, H. Zheng, Improving the generalized Bloch mode synthesis method using algebraic condensation, Comput. Methods Appl. Mech. Engrg. 379 (2021) 113758.
- [46] S. Hajarolasvadi, A.E. Elbanna, Dynamics of metamaterial beams consisting of periodically-coupled parallel flexural elements: a theoretical study, J. Phys. D: Appl. Phys. 52 (2019) 315101.
- [47] V. Cool, L. Van Belle, C. Claeys, E. Deckers, W. Desmet, Impact of the unit cell choice on the efficiency of dispersion curve calculations using generalized Bloch mode synthesis, J. Vib. Acoust. 144 (2022) 024501.
- [48] C. Zhou, J.-P. Lainé, M. Ichchou, Wave finite element method based on reduced model for one-dimensional periodic structures, Int. J. Appl. Mech. 7 (2015) 1550018.
- [49] Y. Fan, C. Zhou, J.-P. Lainé, M. Ichchou, L. Li, Model reduction schemes for the wave and finite element method using the free modes of a unit cell, Comput. Struct. 197 (2018) 42–57.
- [50] C. Droz, C. Zhou, M. Ichchou, J.-P. Lainé, A hybrid wave-mode formulation for the vibro-acoustic analysis of 2D periodic structures, J. Sound Vib. 363 (2016) 285–302.
- [51] T.K. Hasselman, A. Kaplan, Dynamic analysis of large systems by complex mode synthesis, J. Dyn. Syst. Meas. Control 96 (1974) 327–333.
- [52] J.-G. Beliveau, Y. Soucy, Damping synthesis using complex substructure modes and a hermitian system representation, AIAA J. 23 (1985) 1952–1956.
- [53] A. de Kraker, Generalization of the Craig-Bampton CMS Procedure for General Damping, Technical Report, Technische Universiteit Eindhoven, Vakgroep Fundamentele Werktuigkunde, 1993, Rapportnr. WFW 93.023.
- [54] R.R. Craig, Z. Ni, Component mode synthesis for model order reduction of nonclassically damped systems, J. Guid. Control Dyn. 12 (1989) 577–584.
- [55] A. de Kraker, D.H. van Campen, Rubin's CMS reduction method for general state-space models, Comput. Struct. 58 (1996) 597-606.
- [56] M.H. Liu, G.T. Zheng, Improved component-mode synthesis for nonclassically damped systems, AIAA J. 46 (2008) 1160-1168.
- [57] F.M. Gruber, D.J. Rixen, Comparison of Craig–Bampton approaches for systems with arbitrary viscous damping in dynamic substructuring, Dyn. Coupled Struct. 4 (2018) 35–49.

- [58] F.M. Gruber, D. Berninger, D.J. Rixen, Overview of free interface substructuring approaches for systems with arbitrary viscous damping in dynamic substructuring, Dyn. Substruct. 4 (2020) 101–131.
- [59] D. De Domenico, G. Ricciardi, Dynamic response of non-classically damped structures via reduced-order complex modal analysis: Two novel truncation measures, J. Sound Vib. 452 (2019) 169–190.
- [60] Z. Ding, H. Li, G. Zou, J. Kong, Considering higher-order effects of residual attachment modes in free-interface component mode synthesis method for non-classically damped systems, J. Sound Vib. 469 (2020) 115129.
- [61] M. Sigalas, E.N. Economou, Band structure of elastic waves in two dimensional systems, Solid State Commun. 86 (1993) 141-143.
- [62] M.S. Kushwaha, P. Halevi, L. Dobrzynski, B. Djafari-Rouhani, Acoustic band structure of periodic elastic composites, Phys. Rev. Lett. 71 (1993) 2022.
- [63] Z. Liu, X. Zhang, Y. Mao, Y.Y. Zhu, Z. Yang, C.T. Chan, P. Sheng, Locally resonant sonic materials, Science 289 (2000) 1734–1736.
- [64] R.F. Boukadia, C. Droz, M. Ichchou, W. Desmet, A Bloch wave reduction scheme for ultrafast band diagram and dynamic response computation in periodic structures, Finite Elem. Anal. Des. 148 (2018) 1–12.
- [65] W. Larbi, J.F. Deü, R. Ohayon, Vibroacoustic analysis of double-wall sandwich panels with viscoelastic core, Comput. Struct. 174 (2016) 92–103.
- [66] Y. Wu, K. Yu, L. Yang, R. Zhao, X. Shi, K. Tian, Effect of thermal stresses on frequency band structures of elastic metamaterial plates, J. Sound Vib. 413 (2018) 101–119.
- [67] Y. Waki, B.R. Mace, M.J.J. Brennan, Numerical issues concerning the wave and finite element method for free and forced vibrations of waveguides, J. Sound Vib. 327 (2009) 92–108.